TU Delft

UMC Utrecht

Technical Errors in a Novel Mixed Reality Navigation System for Orthopedic Implant Surgery

R.M. van Bakel

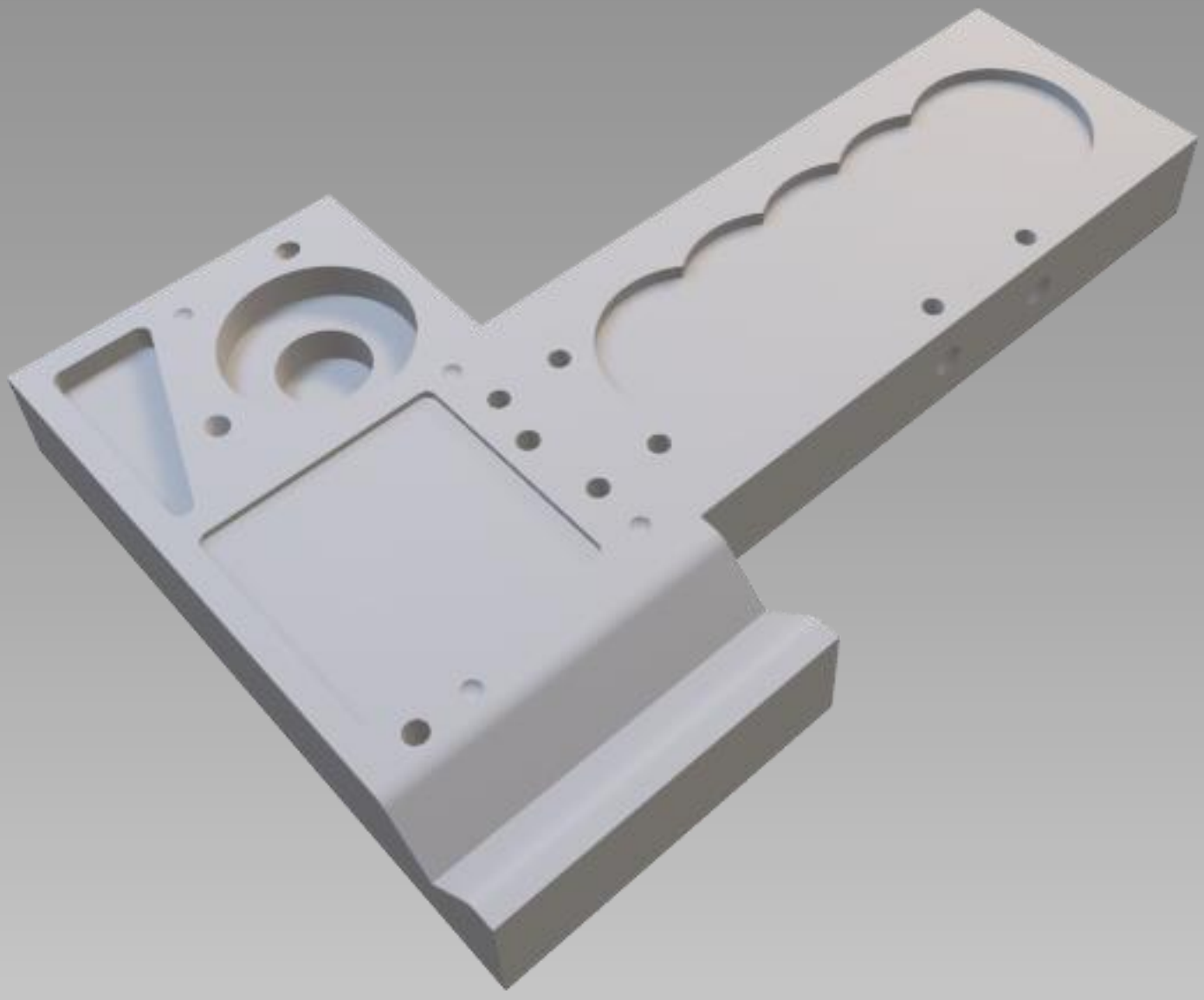

----- This page is intentionally left blank -----

TECHNICAL ERRORS IN A NOVEL MIXED REALITY NAVIGATION SYSTEM FOR ORTHOPEDIC IMPLANT SURGERY

Roan Miquell van Bakel

Student number : 4654021

14th February 2024

Thesis in partial fulfilment of the requirements for the joint degree of Master of Science in

Technical Medicine

Leiden University ; Delft University of Technology ; Erasmus University Rotterdam

Master thesis project (TM30004 ; 35 ECTS)

Dept. of Orthopedic Surgery, UMC Utrecht

7th June 2023 – 28th February 2024

Supervisor(s):

Prof. dr. ir. Harrie Weinans

Dr. Bart van der Wal

Chien Nguyen, MSc

Thesis committee members:

Prof. dr. ir. Harrie Weinans, TU Delft (chair)

Dr. Bart van der Wal, UMC Utrecht

Chien Nguyen, MSc, UMC Utrecht

Dr. Roy van den Ende, Leiden UMC

Table of Contents

1.Summary

Introduction
An innovative, patient-specific, hip implant was developed for canine patients suffering from developmental hip dysplasia. In a first cohort study, the post-operative positions of the implants deviated with an average of 5 mm when compared to the pre-operatively planned positions. A novel augmented reality (AR) based intra-operative navigation method (Holoma) was proposed to decrease implant positioning errors to a maximum of 3 mm. Holoma provides ArUco marker-based, mixed reality surgical navigation on the Hololens 2. The goal of this study was to quantify the error associated with each technical component in Holoma, to determine its navigational accuracies.

Methods
Holoma's technical errors were quantified in a laboratory setting within a surgical operation room. The accuracy of ArUco marker localization and the amount of jittering (falsely detected marker movement) were tested by performing stationary and dynamic experiments. The precision of three image-to-patient registration methods (marker pose, point-to-point, point cloud) was determined by calculating the euclidean distance between multiple registration attempts. Lastly, implant navigation accuracy was quantified by positioning an implant on a precisely predetermined position and recording Holoma's navigation instructions.

Results
Holoma's ArUco marker localization accuracy had a median error of -0.97 mm (*min; max:* -2.04; -0.27) with a marker-to-camera distance of 60 cm, and median jittering was 0.65 mm (*min; max:* 0; 2.07). Median image-to-patient registration precision was 2.20 mm (*min; max:* 0.39; 6.00), 3.52 mm (0.21; 6.92), and 3.79 mm (0.55; 8.83), for marker pose, point-to-point, and point cloud registration, respectively. Lastly, implant navigation instructions showed median errors of 2 mm (*min; max:* 0; 7), 3 mm (0; 7), and 4 mm (0; 9) after marker pose, point-to-point, and point cloud registration, respectively.

Discussion and conclusion
The experiments suggest an accumulation of technical errors in Holoma's navigation application. The accuracy and precision of the navigation software were determined to be inadequate to decrease patient specific hip implant placement errors, at the time of investigating. Future improvements within Holoma will determine its feasibility for accurate implant navigation. Other navigation techniques should be considered in the search for optimal implant positioning guidance.

2.Introduction

2.1. Clinical relevance

Hip dysplasia is a congenital, progressive disorder where the development of the shape and orientation of the acetabulum is disturbed (3). A dysplastic acetabulum is typically shallow and vertically aligned, compared to a normally developed acetabulum. Therefore, the joint center is lateralized, and the femoral head coverage is lower, which causes a variety of problems and complaints. The most common symptoms of hip dysplasia are pain, hip instability, limited abduction in infants, asymmetric gait in toddlers, and early onset of hip osteoarthritis in adults (3). The incidence of congenital hip dysplasia is population specific, but varies between 0,5% and 6,8% for the adult Caucasian population (4).

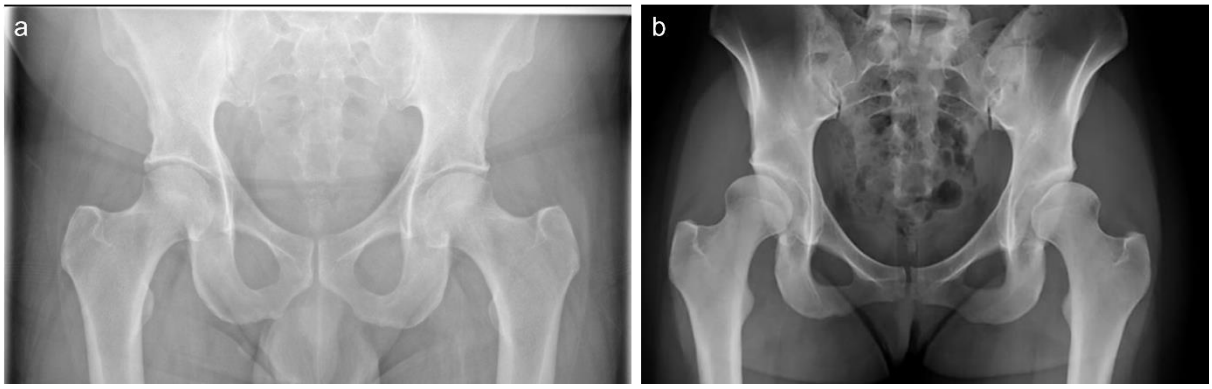

Figure 1 Röntgen image of healthy pelvis (left) and of a patient suffering from developmental hip dysplasia (right) (1, 2). Both the left and right acetabulum of the hip dysplactic patient are shallow and vertically aligned, allowing for less femoral head coverage.

Non-surgical treatments for congenital hip dysplasia are most effective when the disorder is diagnosed in infants, before the age of 7 weeks (5, 6). A common non-surgical treatment in children is the splint appliance, which secures the hip in flexion and abduction (7). There exists a variety of surgical procedures for adults and adolescents with hip dysplasia, such as the periacetabular osteotomy (PAO), also known as the Ganz osteotomy, the Staheli shelf acetabuloplasty, the Chiari osteotomy, and the Pemberton acetabuloplasty (8-12). The common goals of the different surgical procedures are to normalize biomechanics of the hip joint, increase joint contact area, slow down development of osteoarthritis, and increase stability (8). These interventions are invasive, technically complicated, and with a high risk of complications (13).

Not only human, but other animals suffer from congenital hip dysplasia as well. Hip dysplasia in the dog, for example, comes with similar symptoms and (radiographically) signs when compared to human patients (14). Depending on the breed, the prevalence of canine hip dysplasia was found to be almost 20% (15). Willemsen et al. described the similarities between canine and human patients, based on the anatomy, physical examination, radiographical signs, and treatment options (14). Based on these findings, a new treatment has been developed for canine hip dysplasia. The treatment is based on a patient specific, 3D printed implant, which should extend the acetabular rim, and therefore increase the femoral head coverage (16).

The early clinical results are very promising when focusing on biocompatibility, relieving pain, radiographical rim extension, and restoring hip joint stability (17, 18). However, the placement of the patient specific implants tends to be a difficult task for the surgeon. The

limited field of view of the surgical area, growth of the dog between implant design and surgery, and the presence of soft tissues (hard to detect on CT) with unknown shapes and sizes, makes the precise positioning of the implant a challenging task.
In an attempt to overcome these limitations, intra-operative fluoroscopy is utilized to confirm correct positioning of the implant, still with the limitations of 2D imaging (18). In addition, some patients will receive a bilateral implant, making the fluoroscopy even more difficult to interpret. Pre-published study results on the accuracy of implant positioning, suggest a mean translational and rotational placement error of approximately 5 mm and 8 degrees, respectively, when comparing the positioned implant with the pre-operative plan. Literature suggests that patient-specific instruments could be accurate within a range of 2 to 3 mm, which is more difficult to achieve in pelvic regions (19-27).
A new approach in the form of intra-operative augmented reality (AR) navigation was suggested to increase placement accuracy. AR in orthopedic surgery has gained attention in the last few years, with focus on screw placement, osteotomy guidance, oncological resection, and spinal procedures (28). 3D virtual images can be superimposed onto the users field of view, using a head-mounted display. Displaying patient specific models can guide the surgeon during the procedure and makes it possible to see surrounding anatomical structures outside the direct surgical area during surgery. The position and orientation of instruments, implants, or any other surgical tools can be tracked in space and visualized to the user.
A specific novel AR based system, called Holoma (ICM-B, Bulgaria), was available for the UMC Utrecht since its early stage, and was developed with the purpose of surgical navigation. The AR navigation is provided as an application on the Hololens 2 (Microsoft, USA), and uses ArUco markers to track instruments and perform image-to-patient registration. It was originally created for drill and saw guidance during surgery but was recently expanded to support more accurate implant positioning as well.

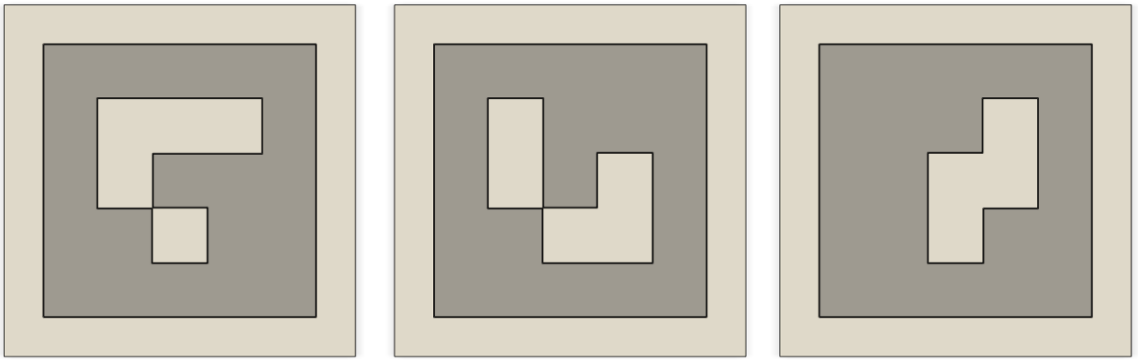

Figure 2 Three types of ArUco markers supported by Holoma. The markers are typically made out of white plastic with black paint or plastic on top of it, or made from anodized metal.

Holoma might be able to reduce the current placement error of 5 mm in patient-specific canine hip implants. The final goal was to reduce overall implant positioning errors to a maximum of 3 mm (19-27). Whether or not Holoma's intra-operative navigation had the potential to accommodate for this need, remained unclear. This thesis provides a quantitative analysis to validate Holoma's accuracy and precision.

2.2. Research question and goal

This thesis aimed to answer the following research question:

Is Holoma's AR based surgical navigation application sufficiently accurate to enhance canine patient-specific hip implant positioning?

The final navigation accuracy is an accumulation of technical uncertainties and errors within the application's workflow. This study aims to identify the technical components and quantify the error contributions of each component within Holoma.

2.3. Technical background

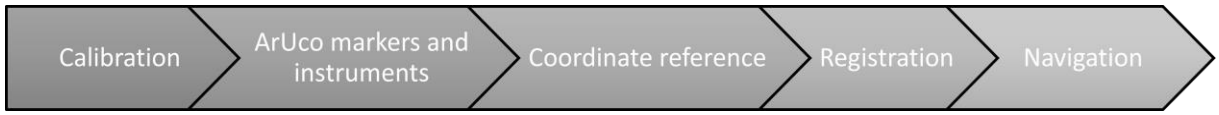

Figure 3 Holoma's technical workflow to accommodate implant navigation.

Figure 3 provides an overview of the main steps that contribute to Holoma's navigation error. Each step in this navigation pipeline will be described in more detail.

2.3.1. ArUco marker localization

ArUco markers are a fundamental component in Holoma's navigation application. The ArUco markers consist of black and white frames, with the black segment measuring 35x35mm. The markers are detected by the front camera of the Hololens and the 3D location and orientation are determined based on the markers shape and size. Holoma's ability to detect and accurately determine a marker's relative location in 3D space is a critical functionality. Figure 2 and figure 5a illustrates examples of various supported ArUco markers.

2.3.2. Calibration

Holoma calculates the distance between the camera and an ArUco marker based on its relative size in an image. Holoma's calibration process determines the relationship between the size of a marker on an image, and its distance to the camera (depth). This relationship is variable for different environments, as the amount of light can affect the detectability of the ArUco markers.
To perform calibration, a pair of identical-sized ArUco markers needs to be positioned at a known and fixed distance from each other. While the two markers remain stationary, the user moves fluidly towards and away from the markers, incorporating lateral movements to conduct the calibration process.

2.3.3. ArUco marker tracking

After detecting an ArUco marker and determining its 3D location, precise and real-time tracking of the marker becomes crucial. Continuous detection of an ArUco marker while the Hololens is attached to a user's head introduces some challenges. Optimal outcomes depend on Hololens stability, an appropriate viewing angle, and maintaining an ideal marker-to-camera distance - three properties that might be challenging for the user to

maintain. Holoma continuously utilized these three criteria to determine the localization confidence level. Figure 5b provides a visual representation from the user's perspective during high-confidence ArUco detection and localization.

2.3.4. Instrument tracking

Holoma facilitates the tracking and visualization of instruments during (surgical) procedures. It is essential to define the exact positions of each ArUco marker in relation to the rest over every instrument, before a procedure. Intra-operative detection of an ArUco marker is used to determine the orientation and position of a specific instrument in real time. Instruments such as a drill or bone saw can be navigated and visualized to the user.

An important instrument that is crucial in most procedures is the registration pointer. The registration pointer is a straight, metal pointer with an ArUco marker attached to it. The length of the pointer is 120,5 mm, measured from the pointer's tip to the center of the ArUco marker's surface. Figure 4 provides more detailed specifications. The pointer is a main component for image-to-patient registration, where a virtual model is matched to the real patient. The accurate localization of the pointer's tip in 3D space is an essential component for accurate image-to-patient registration. An ArUco marker is therefore tightly attached to the pointer.

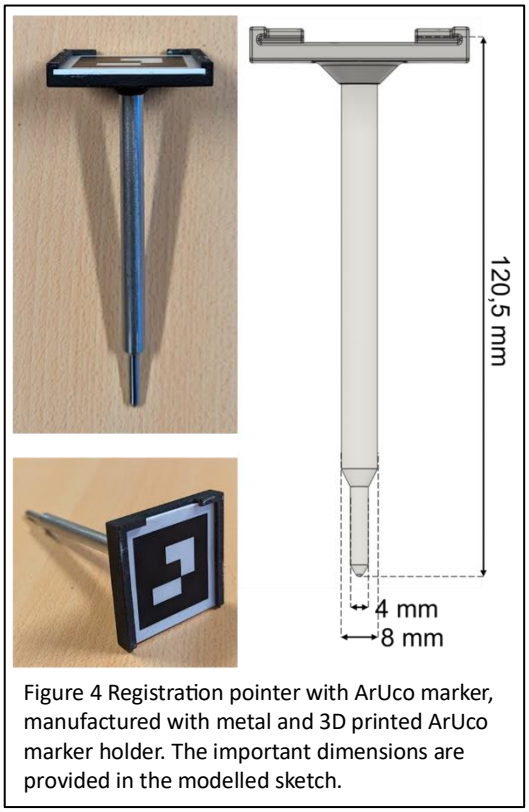

Figure 4 Registration pointer with ArUco marker, manufactured with metal and 3D printed ArUco marker holder. The important dimensions are provided in the modelled sketch.

Brainlab – instrument tracking

An alternative method of tracking a registration pointer is presented by Brainlab, a system commonly used in surgical (neuro)navigation (29). The system consists of a dual infrared camera, enabling the detection and localization of surgical instruments through spherical passive reflective infrared fiducial markers. The markers are fixed onto an instrument, and the known relation between the fiducial markers an each instrument, enables the system to precisely determine the position and orientation of an instrument in real time. According to Brainlab's technical documentation, the reported 3D localization accuracy of such spherical fiducial markers is <=2.0 mm (30).

2.3.5. Hololens' coordinate system

The Hololens is equipped with a built-in feature that continually monitors its surroundings, facilitating the creation and maintenance of a spatial coordinate system (31, 32). Using multiple sensors, the Hololens captures details of its surrounding to anchor a coordinate system to real-world objects. As a user moves, the Hololens performs corrections to maintain a stationary coordinate system. Inadequate performance of these corrections can result in coordinate system 'drift', causing holograms attached to this coordinate system to experience drift or jumps as well.

To reduce the effect of this issue, Holoma introduces a functionality to utilize a custom coordinate system anchor: a 70x70 mm ArUco marker. Positioned at a fixed location and consistently within the field of view of the Hololens through a procedure, this marker should reduce the risk of coordinate system drift, ensuring hologram positional stability.

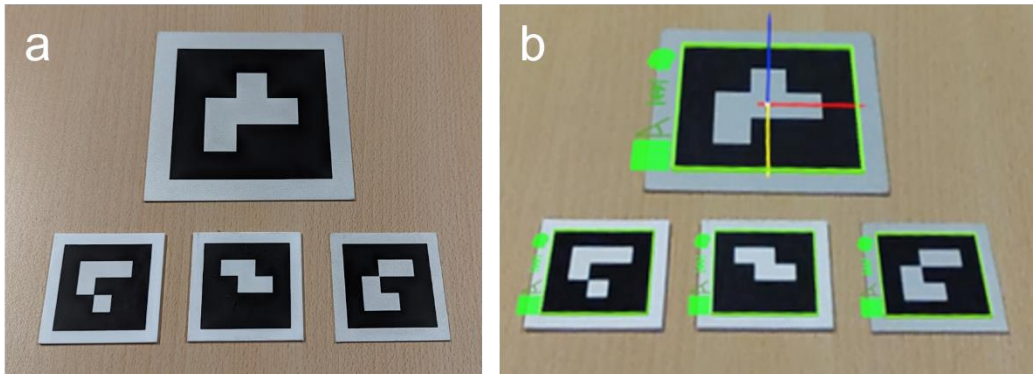

Figure 5 a) Image of the real-life manufactured metal ArUco marker supported by Holoma. A 70x70mm marker represents the origin of a custom coordinate system. b) Illustrates a user's perspective of confident marker localization when wearing the Hololens.

2.3.6. Image-to-patient registration

Accurate assessment of the 3D position and orientation of a patient is crucial for effective surgical navigation. Image-to-patient registration aligns the preoperative surgical plan with the real-world intra-operative view. Holoma offers three registration methods: Marker Pose, Point-to-Point, and Point cloud registration.

Marker Pose involves the predefinition of the location and orientation of an ArUco marker in relation to the patient. Given the fixed relation, detection of the predefined ArUco marker enables intra-operative registration.

Point-to-point registration requires an intra-operative localization of a set of predefined points. Defining these points on anatomical landmarks makes intra-operative identification seamless and reliable. The registration pointer is used to transfer the points' real-life positions into virtual coordinates.

Point cloud registration also utilizes the registration pointer but requires the collection of a surface area instead of a predefined set of points. This surface area is determined in the pre-operative plan, and should have clear boundaries, existing curvatures, and a unique shape. By tracing the surface with the registration pointer, the predefined surface area is matched with the collected datapoints.

Furthermore, Holoma makes use of a patient reference marker, which is attached to the patient. The goal of this reference marker is to move virtual objects along with the patient, in case the patient moves after image-to-patient registration is performed.

2.3.7. Implant navigation

Importing an implant – fixed to an ArUco marker as an instrument in Holoma – enables continuous, real-time 3D tracking of the implant. After image-to-patient registration is performed, users receive instruction to orient the implant to a specific location to align it with the predetermined, desired position from the pre-operative plan. Holoma provides the user with instructions to move the implant into a certain direction for a specific distance in millimeters.

3.Methods

To assess Holoma's navigation software accuracy and precision, experiments were conducted in a controlled laboratory setting. The experiments were designed to isolate specific technical error contributors within the navigation pipeline, as depicted in Figure 3. The following sections will elaborate on the conducted tests and the predefined primary outcomes.

3.1. ArUco marker localization accuracy and calibration reproducibility

The following tests aimed to determine the reproducibility of the calibration process, as well as the ArUco marker localization accuracy. The primary outcome was the error in Holoma's distance measurements between two fixed ArUco markers post-calibration. The absolute median of these errors determined the localization accuracy of an ArUco marker pair, while the range in errors determined the calibration precision (reproducibility).

Two ArUco markers were inserted into a 3D printed calibration setup, and calibration was performed multiple times (n=6). The highest and lowest observed distances between the two markers were recorded. The Hololens remained completely stationary during the measurements.

Measurement errors were recorded for marker to camera distances of 25cm, 40cm, and 60cm to quantify accuracy of ArUco marker depth estimations after calibration. Additionally, measurements were performed in regular lighting conditions and compared to overhead surgical lights illuminating the ArUco markers, to quantify the influence of lighting conditions on the marker localization accuracy and the calibration reproducibility.

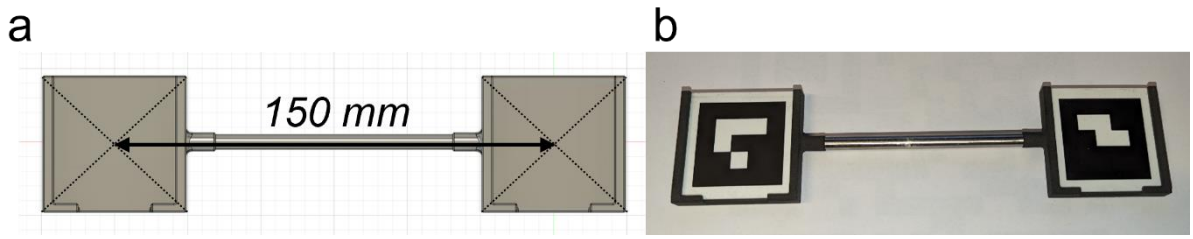

Figure 4 Calibration setup with two ArUco markers attached to each other with a fixed distance. A) shows the design, and B) shows the manufactured product.

3.2. ArUco marker and registration pointer tracking

The following experiments aimed to assess the stability and precision of Holoma's marker detection and localization algorithm. The primary outcome was the amount of jittering, defined as falsely detected movements of a stationary ArUco marker and registration pointer in 3D space. The 3D coordinates of a stationary ArUco marker and the attached registration pointer, were recorded over a short period of time, and because the marker was stationary, any detected movement or displacement was an indication for the localization error. The amount of jittering was determined by calculating the euclidean

distance in mm for every recorded 3D position, relative to its starting position, and determining the range in falsely detected movements. The difference in jittering between the ArUco marker and the pointer's tip was calculated to determine the additional error that is introduced because of the 120.5 mm arm between the marker and the pointer's tip.

Marker localization stability and precision were quantified for different ArUco marker materials (plastic, plastic with matte coated paint, and anodized metal). The error introduced by Hololens movement was determined by conducting the experiments with different Hololens motions. Tests were performed with a stationary Hololens, a user wearing the Hololens while standing as stationary as possible, and a user wearing the Hololens while moving its head left to right, forwards and backwards, or up and down.

Additionally, experiments were performed to quantify the 3D localization precision of a dynamic registration pointer. In these tests, the 3D location of a rotating pointer's tip was recorded, while the pointer's tip remaining in a fixed position. Three experiments were conducted: rotating small circles while the Hololens was stationary, rotating larger circles while the Hololens remained stationary, and rotating small circles while the user was wearing the Hololens and remained as stationary as possible. To ensure a stationary position of the pointer's tip, a special device was used, depicted in figure 7.

Holoma's 3D localization precision of the pointer's tip was compared with Brainlab's. Three experiments were conducted to compare Brainlab's registration pointer localization precision with Holoma's. 3D coordinates of Brainlab's registration pointer were recorded while the pointer and camera remained stationary, while the pointer was rotating with the tip remaining on a fixed position, and while the pointer was stationary and the camera made left-to-right motions.

Figure 5 Registration pointer with a device that keeps the tip in a stationary 3D position, while rotating the pointer.

3.3. Coordinate anchor stability

Experiments were conducted to assess the accuracy and precision of Holoma's coordinate system anchor functionality when a user walked around an object. The primary outcome was the 3D positioning of an object registered with marker pose relative to a stationary

coordinate system anchor. Marker pose registration was performed from five different user positions encircling a stationary object, with a consistent distance between the camera and the object. Euclidean distances and rotational differences among all registered objects were calculated, and then compared to control measurements. The control involved marker pose registration performed 10 times from a stationary user position, and determined the intrinsic precision for marker pose registration. In both sets of experiments, simultaneous visibility of the registration marker and the coordinate anchor marker was ensured.

3.4. Image-to-patient registration

The goal of the following experiment was to determine the precision and accuracy of the three available registration methods. The precision assessment for each registration method consisted of performing each registration method ten times. The positional precision for each registration method was determined by calculating the euclidean distance between all ten registered objects. The orientational precision was assessed by comparing the rotational differences over the x-, y-, and z-axis between the ten registered objects. The accuracy of the point-to-point and point cloud registration methods was determined by comparing the positions and orientations of the registered objects with a control measurement. The marker pose registered object was set as control measurement, as this registration methods is solely reliant on the detection and localization of a single ArUco marker.

Additional experiments were performed to validate the consistency of the patient reference marker. Each registration method was performed ten times with, and ten times without a patient reference marker attached to the registration object. The same ArUco marker was deployed for marker pose registration and as patient reference marker. Precision and accuracy was calculated for both sets of experiments.

A custom object was designed in Fusion 360 to enable consistent performance of the three different registration methods. The designed object aimed to facilitate clear and reproducible features to minimize user-induced errors. For each registration method, a specific feature was included on the custom object. For marker pose registration, a narrow groove was designed to tightly fit an ArUco marker, minimizing the risk for potential movement. Four holes to narrowly fit the registration pointer and four superficial pits were included for precise point-to-point registration. To perform point cloud registration, three distinctive surface sections were included. Figure 8 highlights the key components in the design. The designed object was 3D printed by a UV-resin

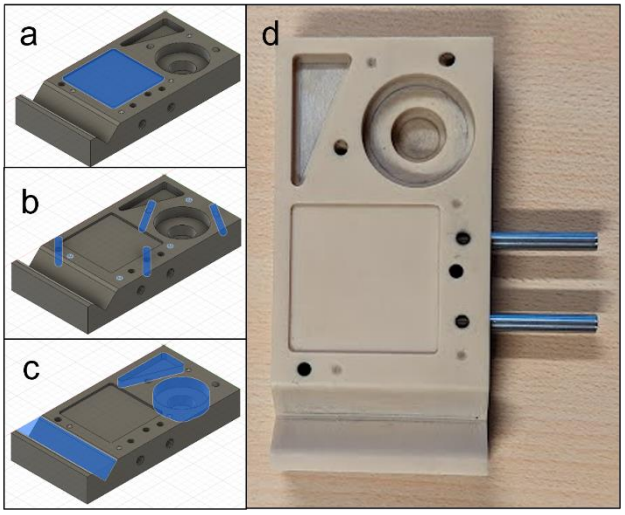

Figure 6. Design and manufactured (3D printed) product of a registration test setup. Regions are dedicated to a specific registration method: a) marker pose, b) point to point, and c) point cloud. The final product d) was employed during the image to patient registration accuracy and precision experiments.

printer (5100 NextDent, 3D Systems) with a layer thickness of 50 micron, and a printing resolution of 65 micron.
Appendix A shows the design process of the registration object.

3.5. Implant navigation

The aim of the implant navigation experiments was to evaluate Holoma's navigation accuracy and precision using a simplified circular implant. To facilitate this, we designed and manufactured a 3D-printed navigation attachment to fixate an ArUco marker to the implant. A virtual representation of the implant with ArUco marker was created through a cone beam CT (CBCT), and imported as an instrument in Holoma. Figure 9 shows the implant with navigation accessory used during the experiments.

Two distinct experiments were conducted to evaluate Holoma's navigational capabilities: tight-fit and no-fit navigation tests. To perform these experiments, an additional object was designed in Fusion 360 and 3D printed, and attached to the previously described registration object. This additional object was created with specific features to conduct the tight-fit and no-fit navigation experiments. Appendix A illustrates the design process of the attached navigation object.
The primary objective of the tight-fit experiments was to assess the disparity between an ideally positioned implant and the navigation instructions provided by Holoma. For this purpose, five circular grooves were manifested into one of the 3D printed object's faces. In the pre-operative plan, the desired positions of the circular implant were precisely determined to be within these grooves. Once the implant was positioned, any navigational instructions served as indication for the navigation error. Participants documented the range of navigation instructions during the experiments. Holoma's implant navigation separated the navigation instructions in two separate directions: perpendicular (depth) and parallel (x/y plane) to the bone surface. The results of the tight-fit navigation tests were separated accordingly.
Four participants conducted tight-fit navigation experiments, of which two technical medicine students, one orthopedic surgeon, and one veterinary surgeon.

No-fit experiments aimed to assess the navigation accuracy with the addition of user-induced errors. Participants were tasked with placing an implant on the flat side of the 3D-printed object, positioning it as close as possible to Holoma's specified location. The recorded locations of the positioned implants were then compared to the predefined implant positions. No-fit experiments were all conducted after marker pose registration.
One additional no-fit experiment was conducted where no active navigation instructions were provided. The participants had to align the implant with the implants hologram.
Hololens' build-in eye calibration was performed prior to the no-fit experiments.

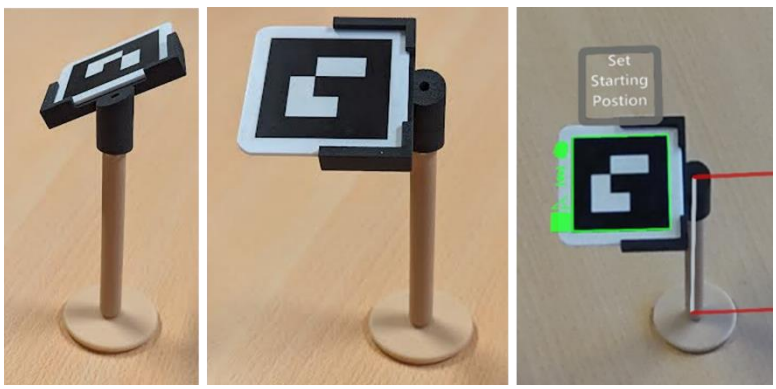

Figure 7 The simplified circular implant with its navigation attachment to facilitate implant navigation.

No-fit navigation experiments were performed by three of the earlier mentioned participants.

Figure 10 illustrates an additional 3D printed navigation object, introduced to extend the previously described registration object. This extension was attachable to the registration part in various locations and orientations.

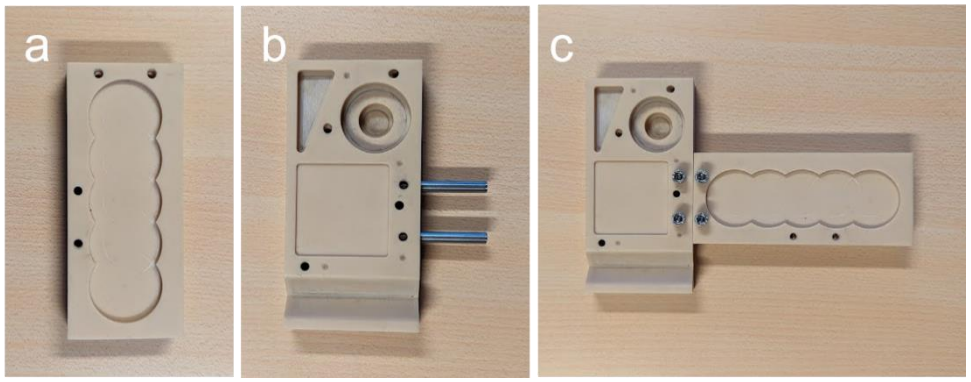

Figure 8 illustrates A) the 3D printed extension, B) the registration setup, and C) the two components combined.

3.6. Statistics

The results from all experiments were presented in boxplots. All results were described in terms of medians, minima, and maxima, after excluding outliers, unless stated otherwise. Outliers were defined as values more than 1.5 * IQR above the third quartile or below the first quartile.

4.Results

4.1. ArUco marker localization accuracy and calibration reproducibility

The measurement errors were -0.06 mm (-0.78; 0.33), -0.81 mm (-1.42; -0.19), and -0.97 mm (-2.04; -0.27) when the markers were 25 cm, 40 cm, and 60 cm away from the camera under regular lighting conditions, respectively. Illuminating the ArUco markers with overhead surgical lights increased measurement errors to 1.7 mm (0.8; 2.6). Figure 11 displays the boxplots of the conducted calibration experiments.

The absolute median errors, and thus the localization accuracy of an ArUco marker pair, was lower at 25 cm when compared to 60 cm away from the camera (0.32 mm vs 0.99 mm, respectively). This accuracy further decreased to 2.23 mm, when overhead surgical lights illuminated the ArUco markers.

The calibration precision, indicated by the ranges of errors, was also lower at closer distances (1.11 mm at 25 cm vs 1.77 mm at 60 cm) under regular lighting conditions. With overhead surgical lights, the calibration precision was 1.8 mm.

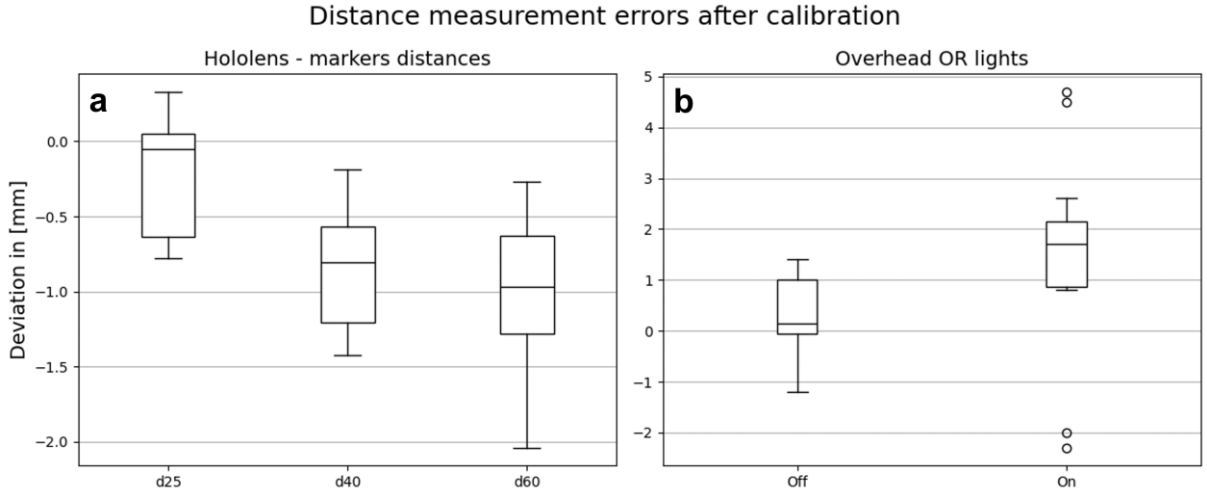

Figure 9. Boxplots of errors in Holoma's distance measurements between two ArUco markers after calibration. Negative values represent an underestimation of the distance between the two markers. The y-axis shows the errors in mm, and the x-axis presents different calibration and measurement scenarios. a) Shows the results of different distances between the Hololens camera and the calibration markers, and b) shows the results of measurements with and without overhead surgical lights on.
d25, d40, d60 = 25cm, 40cm, 60cm between ArUco marker and Hololens camera
Off, On = Overhead surgical lights are off and on

4.2. ArUco marker and registration pointer tracking

4.2.1. Stationary marker experiments

Less jittering was observed for the stationary ArUco marker experiments with a stationary Hololens (*Stationary:* 0.93 mm and *User wearing an Hololens while remaining stationary:* 2.07 mm), compared to experiments involving Hololens motions (*Left-to-right:* 4.46 mm, *Forward-backward:* 4.37 mm, *and Up-and-down:* 10.38 mm). The additional jittering of the registration pointer's tip, caused by the registration pointer's arm of 120.5 mm, varied between 0.21 mm and 4.44 mm in the stationary marker and pointer experiments. Figure 13 and table 1 presents the results for the stationary marker experiments with three different ArUco marker materials.

4.2.2. Dynamic pointer experiments

The amount of falsely detected movement of the pointer's tip in the rotating pointer experiments were 5.49 mm, 6.31 mm, and 4.64 mm while rotating small circles with a stationary Hololens, rotating larger circles with a stationary Hololens, and rotating small circles while the users was wearing the Hololens and remained as stationary as possible, respectively, after combining the data for all three marker materials. Wearing the Hololens reduced jittering for the plastic and matte coated ArUco markers compared to a stationary Hololens, while jittering increased for the metal markers in the same comparison. Figure 14 and table 1 provide the results for the dynamic registration pointer experiments.

4.2.3. Brainlab pointer tracking experiments

Less jittering was observed in all three experiments when comparing falsely detected movements in Brainlab's pointer to Holoma's counterparts (*Stationary pointer and*

stationary camera: 0.27 mm vs 0.93 mm, *Rotating pointer and stationary camera:* 1.22 mm vs 5.49 mm, and *Stationary pointer and camera performing left-to-right motions:* 1.04 mm vs 4.46 mm). Figure 15 and table 1 shows the results of the Brainlab pointer tracking experiments.

Table 1. Results of the ArUco marker and registration pointer tracking experiments, for the three marker materials combined. The median, 1st quartile, 3rd quartile, minimum, maximum, and (inter-quartile) ranges (IQR) are presented in **mm**. ΔRange is the difference in Range between the marker center and pointer end measurements. This serves as indicator for the pointer's tip localization error, caused by determination of the location and orientation of a single ArUco marker.
stat m = Stationary marker, stat c = stationary camera, dyn p(l) = Dynamic pointer (large rotations)

		Observed location	Median	1st quartile	3rd quartile	IQR	Min	Max	Range	ΔRange marker - pointer
Holoma	**stat m - stat c**	*Marker center*	0.44	0.34	0.59	**0.25**	0.00	0.93	**0.93**	**0.37**
		Pointer end	0.65	0.40	0.88	**0.48**	0.00	1.30	**1.30**	
	stat m - stat c user	*Marker center*	0.65	0.58	1.71	**1.13**	0.00	2.07	**2.07**	**0.21**
		Pointer end	0.95	0.61	1.28	**0.67**	0.00	2.28	**2.28**	
	stat m - left/right c	*Marker center*	2.80	2.36	3.63	**1.27**	0.46	4.92	**4.46**	**1.33**
		Pointer end	3.24	2.69	3.64	**0.95**	1.32	4.45	**3.13**	
	stat m - front/back c	*Marker center*	1.68	1.34	2.54	**1.20**	0.00	4.37	**4.37**	**0.30**
		Pointer end	1.97	1.44	2.74	**1.30**	0.00	4.67	**4.67**	
	stat m - up/down c	*Marker center*	1.80	1.00	4.93	**3.93**	0.00	10.38	**10.38**	**4.44**
		Pointer end	1.69	1.08	3.25	**2.17**	0.00	5.94	**5.94**	
Holoma	**dyn p - stat c**	*Pointer end*	2.33	1.58	3.26	**1.68**	0	5.49	**5.49**	
	dyn pl - stat c	*Pointer end*	2.05	1.2	3.26	**2.06**	0	6.31	**6.31**	
	dyn p - stat c user	*Pointer end*	1.95	1.47	2.74	**1.27**	0	4.64	**4.64**	
Brainlab	**stat p - stat c**	*Pointer end*	0.13	0.09	0.18	**0.09**	0.04	0.31	**0.27**	
	dyn p - stat c	*Pointer end*	0.34	0.23	0.89	**0.66**	0.09	1.31	**1.22**	
	stat p - dyn c	*Pointer end*	0.31	0.21	1.04	**0.83**	0.00	1.04	**1.04**	

4.3. Coordinate anchor stability

Both the median and range in euclidean distances were larger in the dynamic experiments, when compared to the stationary control experiments (6.75 mm (3.57; 12.19) vs 1.97 mm (0.28; 5.46), respectively). The rotational differences were also larger in the dynamic experiments in comparison to the stationary experiments, but were exceptionally large for the z-axis (0.85 ° (0.08; 1.62) vs 0.09 ° (0; 0.23)), compared to the x- and y-axis (0.22 ° (0.03; 0.57) vs 0.12 ° (0; 0.44), and 0.27 ° (0.01; 0.44) vs 0.07 ° (0; 0.36), respectively).
Figure 12 shows the results of the custom coordinate system experiments.

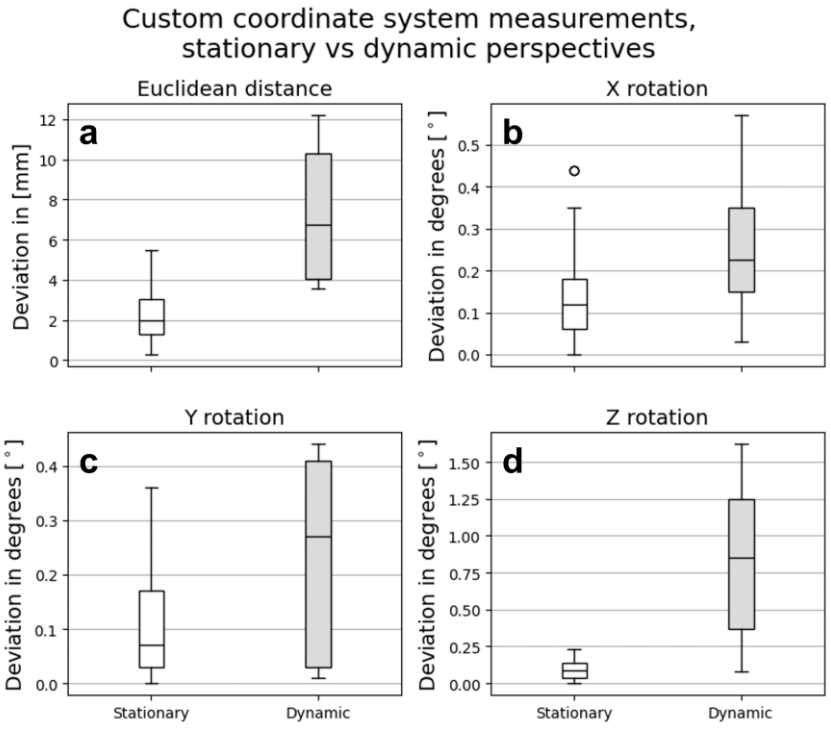

Figure 12. Results of the custom coordinate system experiments. Marker pose registration from a single user's perspective (*Stationary*) were compared to marker pose registrations from different user positions around the object (*Dynamic*). Boxplots show the results of comparing marker pose registration attempts in terms of a) Euclidean distance, b) x-angle rotations, c) y-angle rotations, d) z-angle rotations. All measurements were collected relative to the custom coordinate reference marker.

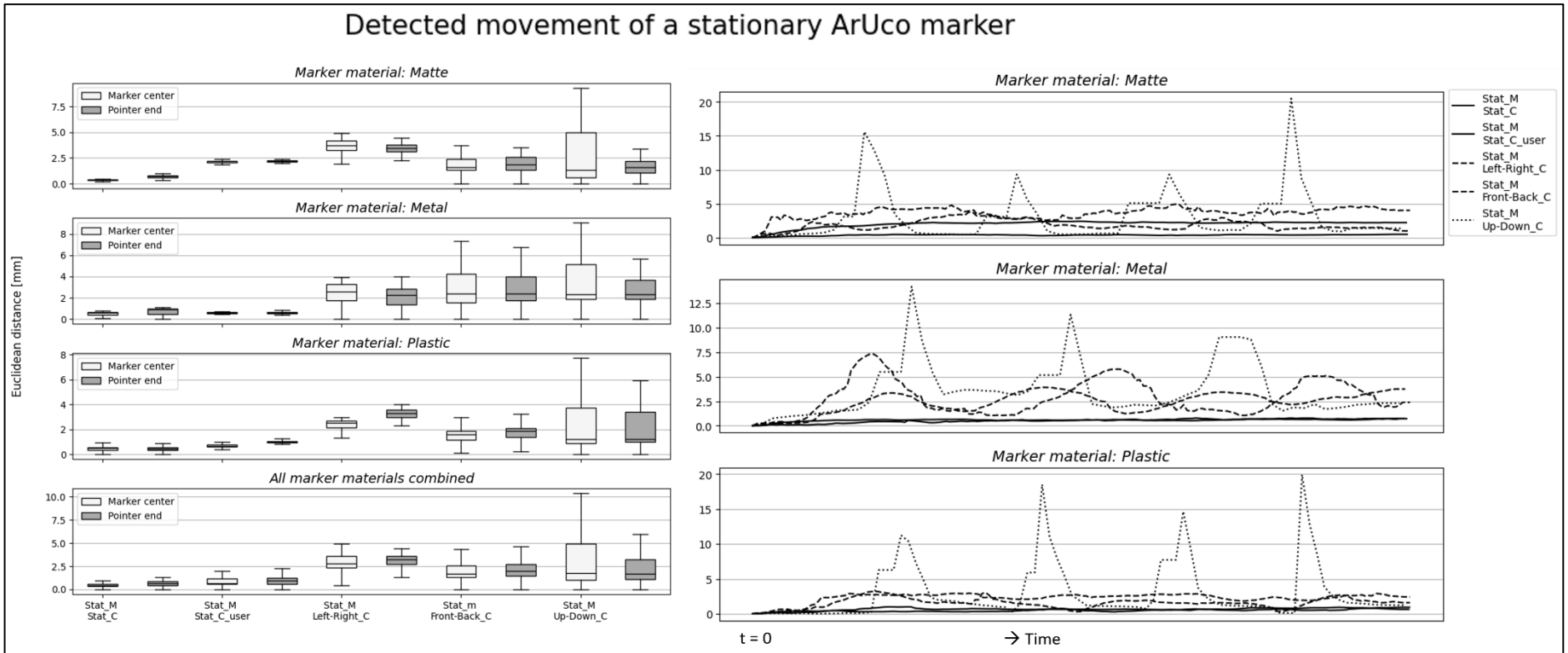

Figure 13. Results of the stationary ArUco marker tracking experiments. The 3D coordinates of stationary ArUco markers were recorded and extracted. The measurements were performed with markers of three different materials. The boxplots (left) show the euclidean distances for five scenarios: stationary camera (*Stat_C*), stationary camera on user's head (*Stat_C_user*), camera movements to the left and right (*Left-Right_C*), forwards and backwards (*Front-Back_C*), and while the user was looking up and down (*Up-Down_C*). The euclidean distances for both the ArUco marker and the registration pointer's tip were calculated. The linegraph (right) shows the original data for the same five scenarios, where the euclidean distances were plotted over time.

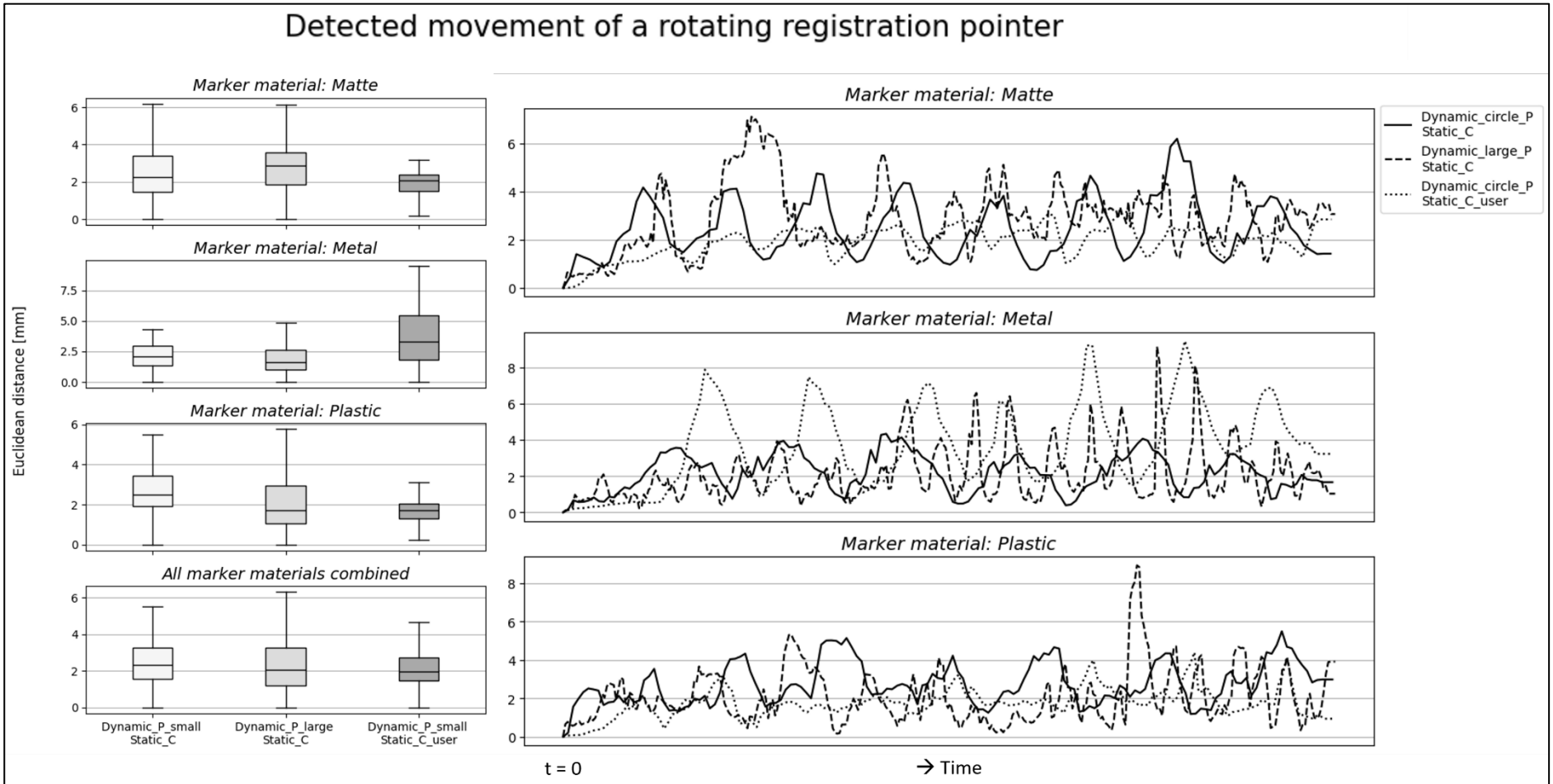

Figure 14. Results of the dynamic registration pointer's tip tracking experiments. The 3D coordinates of a rotating registration pointer were recorded, while the tip remained in a fixed position. The measurements were performed with markers of three different materials. The boxplots (left) show the euclidean distances of the pointer's tip for three scenarios: stationary camera (*Stat_C*) with small (*Dynamic_P_small*) and larger circles (*Dynamic_P_large*), and smaller circles while the camera is stationary on the user's head (*Stat_C_user*). The linegraph (right) shows the original data for the same three scenarios, where the euclidean distances of the pointer's tip were plotted over time.

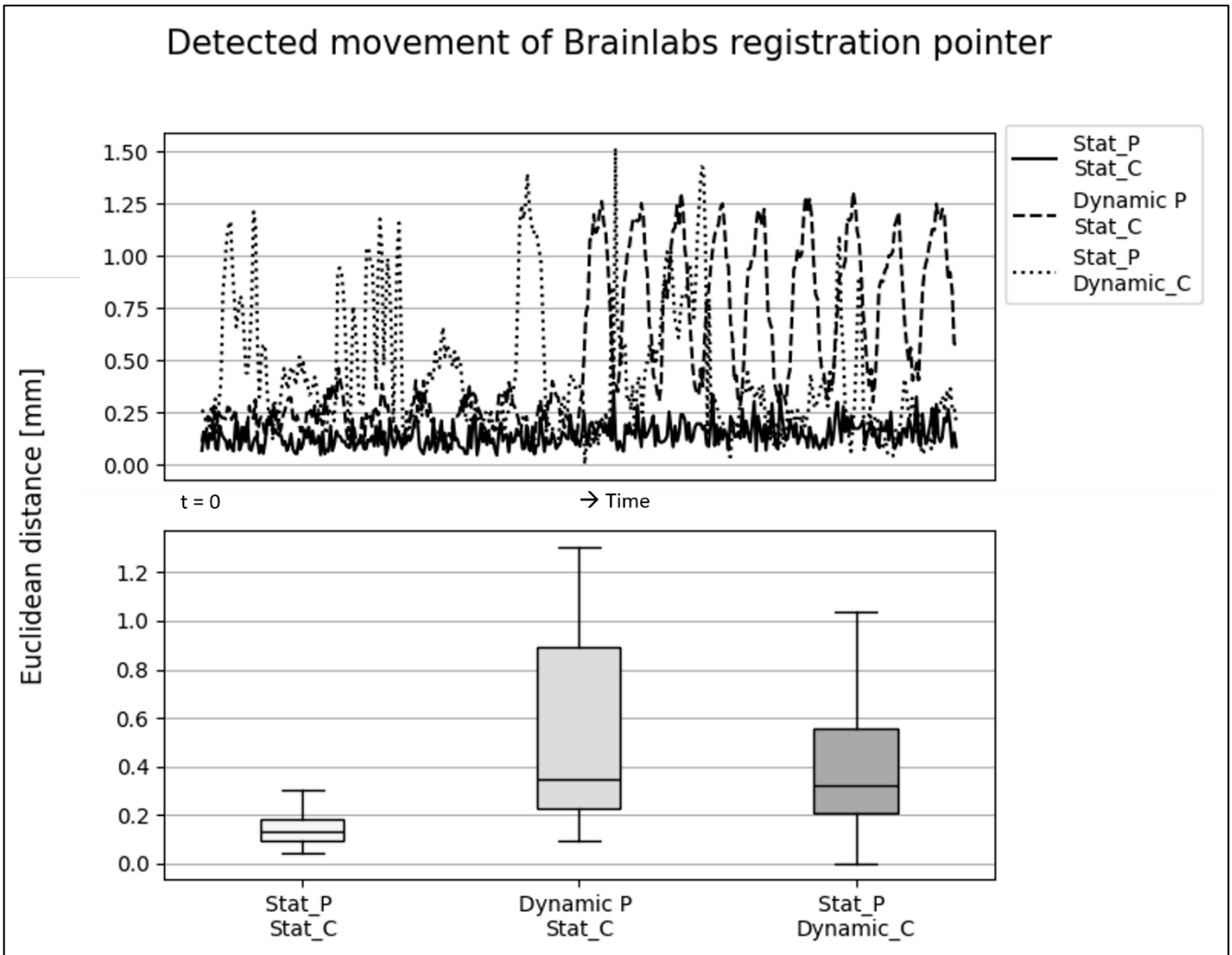

Figure 15. Results of Brainlab's registration pointer precision experiments. The 3D coordinates of the pointer's tip were recorded and extracted. No ArUco marker was involved, as Brainlab detects the registration pointer by detection of infrared reflective markers. The boxplots (lower graph) show the euclidean distances for three scenarios: stationary camera (*Stat_C*) with a stationary pointer (*Stat_P*), and a rotating pointer (*Dynamic_P*), and a stationary pointer with a moving camera (*Dynamic_C*). The euclidean distances for the registration pointer's tip were calculated. The linegraph (upper graph) shows the original data for the same three scenarios, where the euclidean distances were plotted over time.

4.4. Image-to-patient registration

4.4.1. Precision and accuracy without reference marker

The highest positional precision was found in marker pose registration, followed by point-to-point registration, and point cloud registration (*Median (min; max):* 2.20 mm (0.39; 6.00), 3.52 mm (0.21; 6.92), and 3.79 mm (0.55; 8.83), respectively).

Rotational precision and accuracy were lowest for the point-to-point registration in the x- and z-axis when compared to point cloud registrations, while point cloud registration showed lower precision and accuracy in the y-axis. Rotational precision was relatively better in x-, and y-axis for marker pose registration compared to the z-axis.

Figure 16 shows the results of the registration precision and accuracy experiments without the use of a patient reference marker. The medians and corresponding minima and maxima are presented in table 2.

Table 2. Precision and accuracy results for three registration methods without the use of a patient reference marker: marker pose, point-to-point, and point cloud matching. Precisions are computed by comparing positional and rotational parameters within one registration method. Accuracies are computed by comparing positional and rotational parameters point to point and point cloud registrations to the marker pose registrations. Results are presented as median with corresponding minima and maxima in mm.

	Registration method	Eucl distance	X angle	Y angle	Z angle
Precision	*Marker pose*	2.20 mm (0.39; 6.00)	0.15 ° (0; 0.33)	0.04 ° (0; 0.14)	0.33 ° (0.01; 2.79)
	Point to point	3.52 mm (0.21; 6.92)	0.97 ° (0; 3.09)	0.36 ° (0.04; 1.12)	1.18 ° (0.01; 4.61)
	Point cloud	3.79 mm (0.55; 8.83)	0.53 ° (0.04; 1.35)	2.05 ° (0.03; 5.4)	0.61 ° (0.02; 1.76)
Accuracy	*Point to point*	4.18 mm (0.45; 9.26)	0.52 ° (0.01; 2.27)	0.43 ° (0.01; 0.79)	1.34 ° (0; 3.7)
	Point cloud	4.33 mm (0.58; 9.23)	0.65 ° (0.01; 1.28)	1.86 ° (0.33; 2.81)	0.87 ° (0.08; 2.42)

4.4.2. Precision and accuracy with patient reference marker

The addition of a reference marker showed higher precision measurements in terms of euclidean distances for marker pose and point-to-point registrations, while point cloud registration shows worse positional precision.

Rotational precision was slightly worse for point-to-point registration on the x-axis, similar on the y-axis, and slightly better on the z-axis when compared to the experiments without patient reference marker. However, rotational precision was worse for point cloud registration on the x-, y-, and z-axis when compared to the experiments without patient reference marker.

Figure 17 shows the results of the registration precision and accuracy experiments when a patient reference marker was utilized. The medians and corresponding minima and maxima are presented in table 3

Table 3. Precision and accuracy results for three registration methods: marker pose, point to point, and point cloud matching. Precisions are computed by comparing positional and rotational parameters within one registration method. Accuracies are computed by comparing positional and rotational parameters point to point and point cloud registrations to the marker pose registrations. Results are presented as median with corresponding minima and maxima.

	Registration method	Eucl distance	X angle	Y angle	Z angle
Precision	*Marker pose*	1.63 mm (0.55; 4.19)	0.13 ° (0.01; 0.96)	0.15 ° (0; 0.51)	0.28 ° (0.01; 0.90)
	Point to point	2.70 mm (0.63; 9.28)	1.5 ° (0.02; 4.94)	0.33 ° (0.01; 1.17)	0.95 ° (0.0; 3.24)
	Point cloud	8.29 mm (1.19; 73.60)	2.53 ° (0.09; 7.26)	3.73 ° (0.12; 8.45)	4.72 ° (0.07; 19.81)
Accuracy	*Point to point*	2.26 mm (0.29; 8.08)	0.67 ° (0.03; 4.48)	0.37 ° (0; 0.88)	0.59 ° (0; 3.21)
	Point cloud	5.97 mm (0.47; 57.28)	1.47 ° (0; 5.86)	3.19 ° (0.07; 5.16)	1.11 ° (0.03; 19.13)

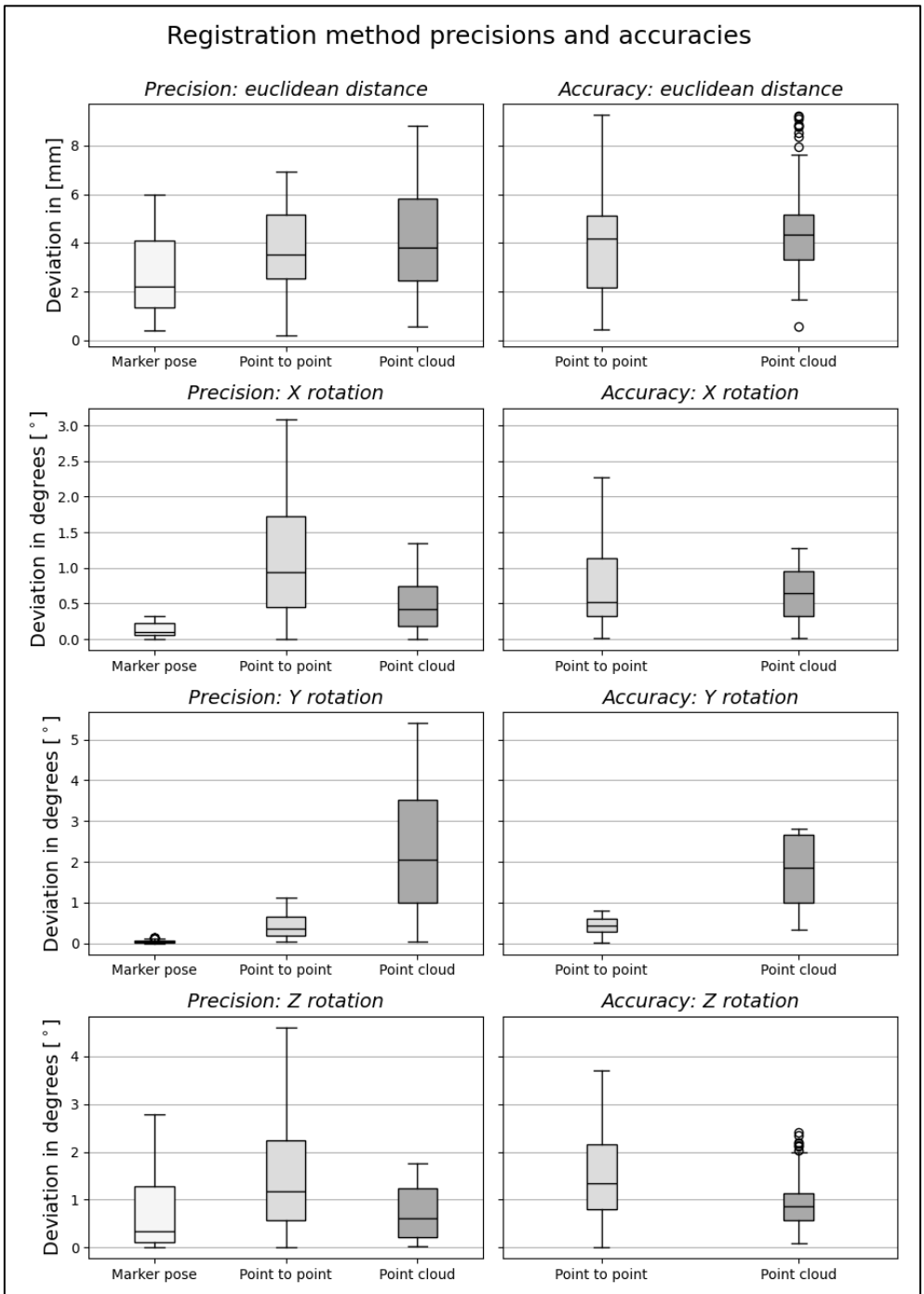

Figure 16. Results of precision and accuracy experiments of three registration methods: marker pose, point to point, and point cloud matching. Precisions are computed by comparing positional and rotational parameters within one registration method. Accuracies are computed by comparing positional and rotational measurements from point to point and point cloud registrations to the marker pose registrations. The positional and rotational parameters are: a+b) euclidean distances and rotations in the c+d) x-, e+f) y-, and g+h) z-axes.

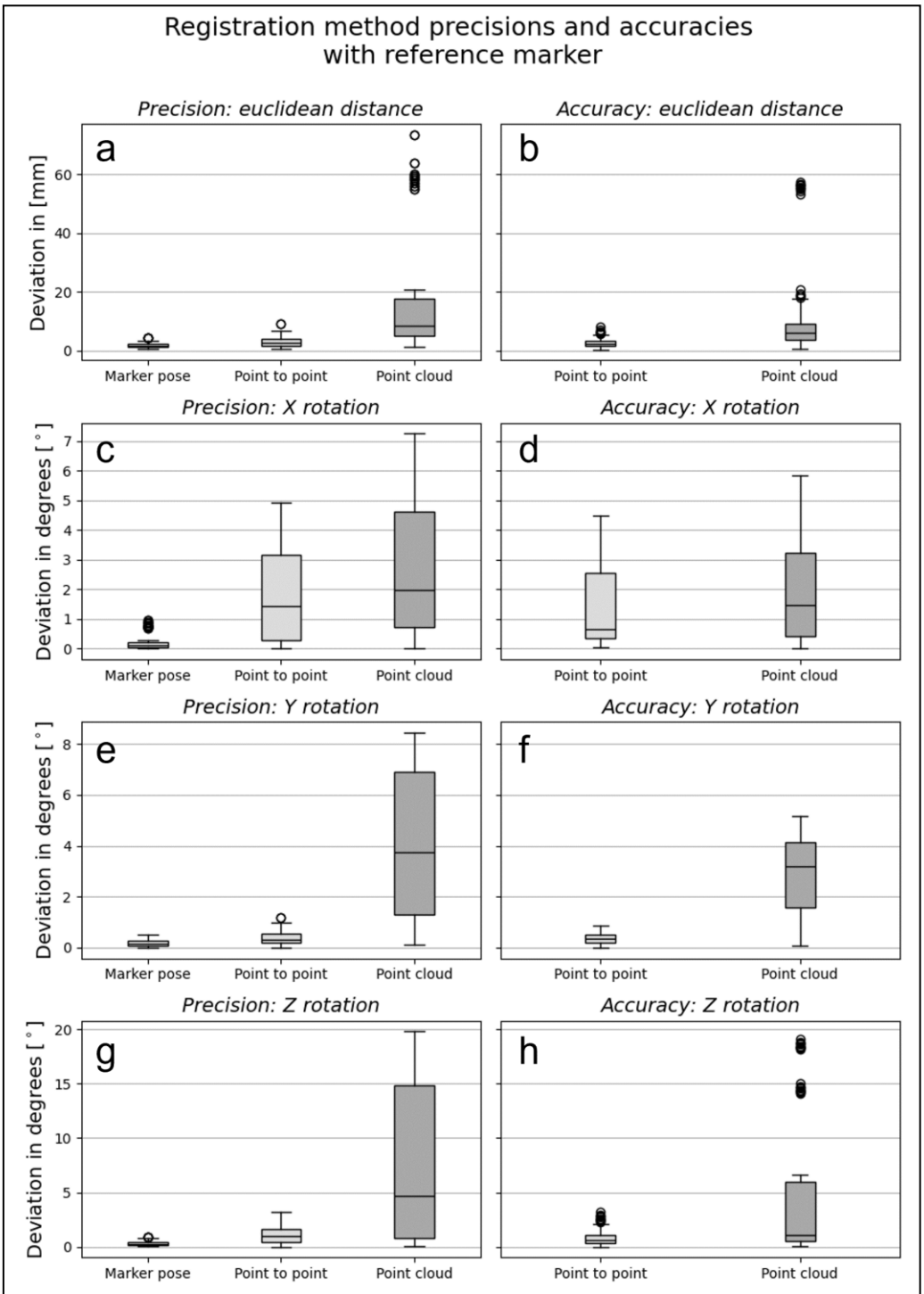

Figure 17. Results of precision and accuracy experiments of three registration methods: marker pose, point to point, and point cloud matching when performed with a reference marker. Precisions are computed by comparing positional and rotational parameters within one registration method. Accuracies are computed by comparing positional and rotational parameters point to point and point cloud registrations to the marker pose registrations. The positional and rotational parameters are: a+b) euclidean distances and rotations in the c+d) x-, e+f) y-, and g+h) z-axis.

4.5. Implant navigation

4.5.1. Tight-fit navigation

The x/y plane navigation errors were lowest for the marker pose registered experiments, followed by the point-to-point and point cloud experiments (*Median (min;max):* 2 mm (0; 7), 3 mm (0; 7), and 4 mm (0;12), respectively).

The observed depth errors were more accurate than the x/y plane error for all three registration methods with navigation errors of 0 mm (0; 2), 1 mm (0; 6), and 0 mm (0; 6) for marker pose, point-to-point, and point cloud registrations, respectively.

The results of all navigation experiments are provided in figure 18 and table 4.

4.5.2. No-fit navigation

The results showed an increase in median positioning errors of 1,14 mm when comparing the active navigated no-fit tests with the tight-fit navigation tests (3,14 mm (0,51; 7,01) vs 2 mm (0; 7)).
The observed placement errors in the no-fit navigation experiments without active navigation were lower compared to the active navigated placements (2,50 mm (0,95; 8,30) vs 3,14 mm (0,51; 7,01)).

The results of all navigation experiments are provided in figure 18 and table 4.

Table 4. Results of tight-fit and no-fit navigation experiments, presented as median (min; max).

	Registration method	Depth error (z-axis)	X-Y plane error
Tight-fit navigation	*Marker pose*	0 mm (0; 2)	2 mm (0; 7)
	Point to point	1 mm (0; 6)	3 mm (0; 7)
	Point cloud	0 mm (0; 6)	4 mm (0; 9)
No-fit navigated	*Marker pose*	-	3.14 mm (0.51; 7.01)
No-fit no navigation	*Marker pose*	-	2.50 mm (0.95; 8.30)

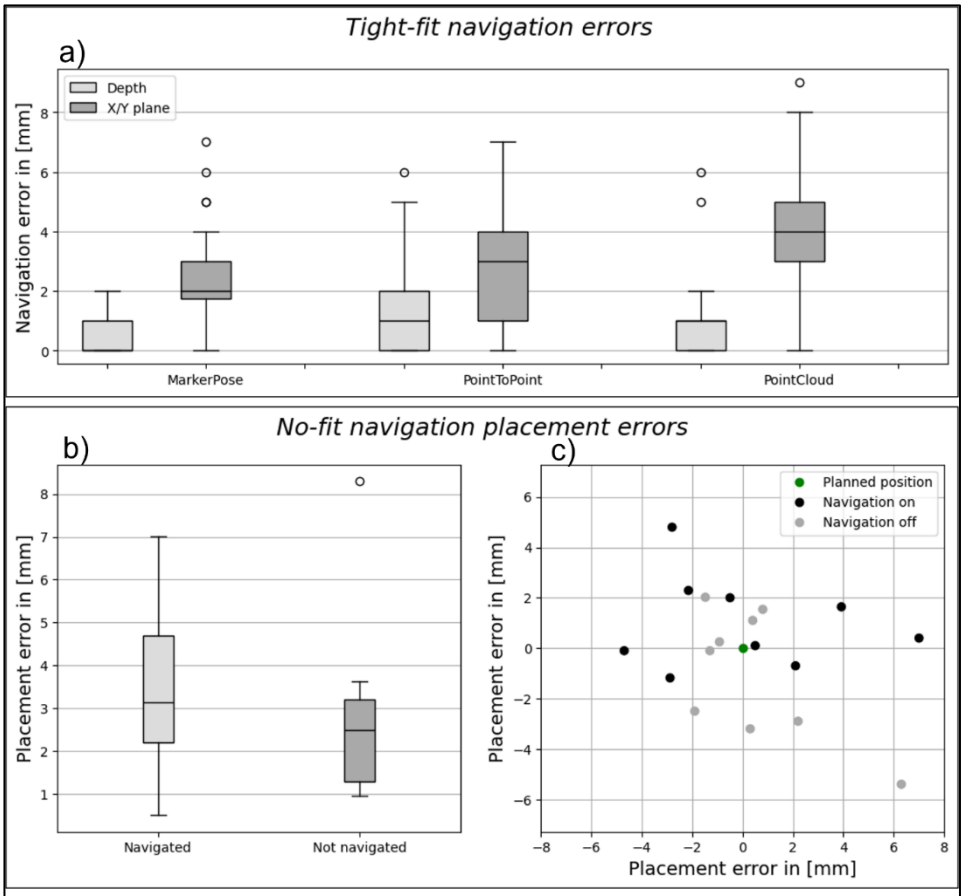

Figure 10. Results of the tight-fit and no-fit navigation experiments. A) shows the results of the depth errors and the x/y plane errors in Holoma's navigation instructions as observed by different participants. B) shows the results of the no-fit navigation placement errors as euclidean distances in boxplot format, while C) depicts the results of the same no-fit experiments with original measurements. The origin (*0, 0*) in image C) is the correct implant position, and the data points are the positions where participants actually positioned the implant, with (black) and without (gray) active navigation.

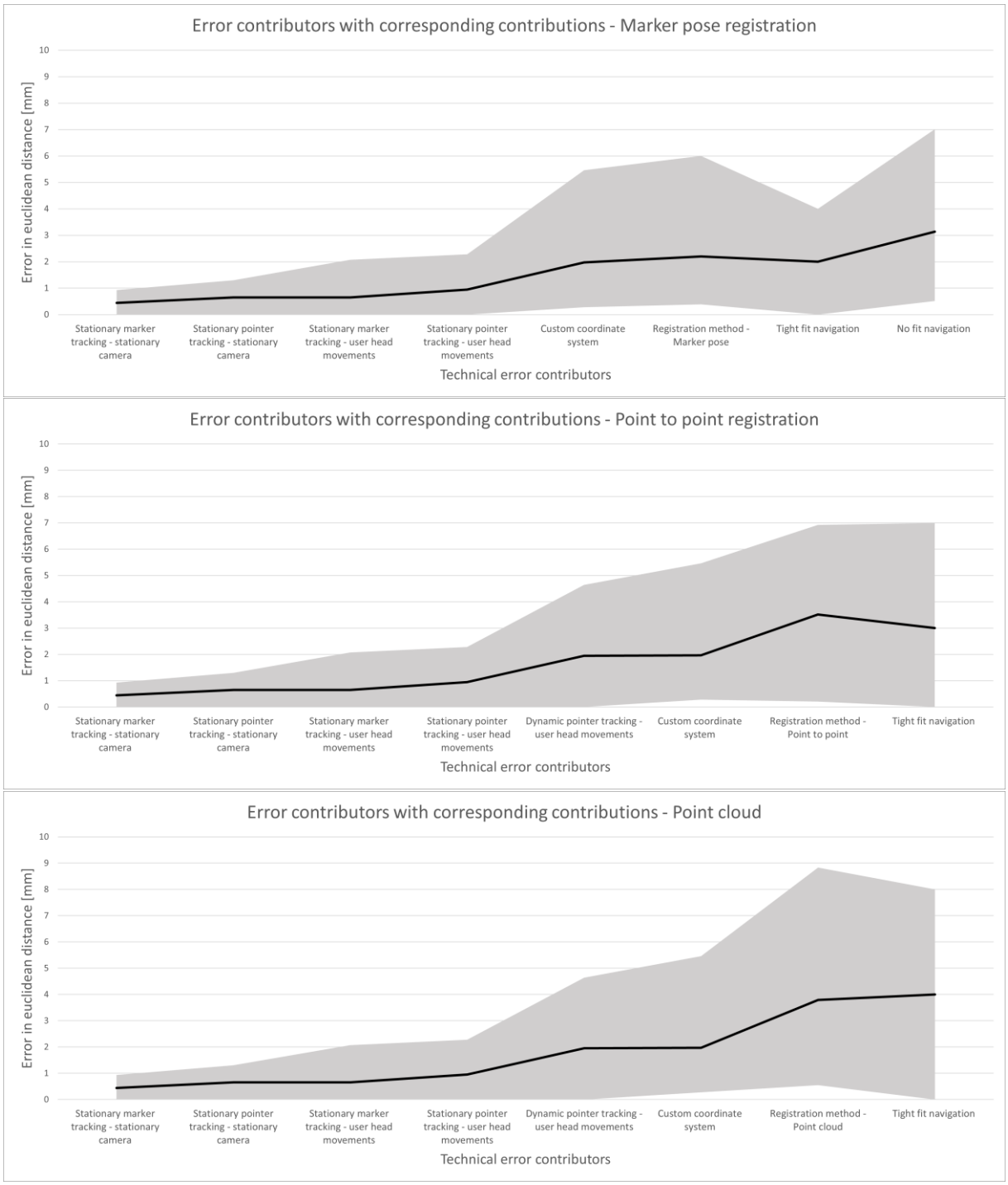

Figure 11 displays the accumulation of median, minimum and maximum errors, as observer per technical component. The observed median errors (black lines) with corresponding ranges (gray regions), excluding outliers, are serially displayed. The error contributors are depicted on the x-axis, and the corresponding error contributions in millimeters are on the y-axis. The error contributors were combined for three registration methods separately (a = Marker pose, b = Point to point, c = Point cloud). The error contributors are not identical for the three registration methods.

Table 5. The results of the different accuracy and precision experiments. The errors for all technical components were summarized in terms of medians with corresponding minima and maxima.

	Measurement	Accuracy/Precision	Scenario	Min	Median	Max
ArUco marker localization - Normal lighting condition	Distance measurement error	Accuracy	*Marker-to-Camera distance = 25 cm*	-0.78 mm	-0.06 mm	0.33 mm
			Marker-to-Camera distance = 40 cm	-1.42 mm	-0.81 mm	-0.19 mm
			Marker-to-Camera distance = 60 cm	-2.04 mm	-0.97 mm	-0.27 mm
ArUco marker localization - OR lights on	Distance measurement error	Accuracy		0.8 mm	1.7 mm	2.6 mm
Stationary ArUco marker tracking	Jittering	Precision	*Stationary camera*	0 mm	0.44 mm	0.93 mm
			Uncontrolled user head motions	0 mm	0.65 mm	2.07 mm
			Active Hololens motions			
			- Left/Right	0.46 mm	2.8 mm	4.92 mm
			- Forward/Backwards	0 mm	1.68 mm	4.37 mm
			- Up/Down	0 mm	1.8 mm	10.38 mm
Stationary registration pointer tracking	Jittering	Precision	*Stationary camera*	0 mm	0.65 mm	1.3 mm
			Uncontrolled user head motions	0 mm	0.95 mm	2.28 mm
			Active Hololens motions			
			- Left/Right	1.32 mm	3.24 mm	4.45 mm
			- Forward/Backwards	0 mm	1.97 mm	4.67 mm
			- Up/Down	0 mm	1.69 mm	5.94 mm
Dynamic registration pointer tracking	Jittering	Precision	*Stationary camera*	0 mm	2.33 mm	5.49 mm
			Uncontrolled user head motions	0 mm	1.95 mm	4.64 mm
Image-to-patient registration - No reference marker	Euclidean distance	Precision	*Marker pose*	0.39 mm	2.2 mm	6 mm
			Point-to-point	0.21 mm	3.52 mm	6.92 mm
			Point cloud	0.55 mm	3.79 mm	8.83 mm
	Rotation over X-axis		*Marker pose*	0 °	0.15 °	0.33 °
			Point-to-point	0 °	0.97 °	3.09 °
			Point cloud	0.04 °	0.53 °	1.35 °
	Rotation over Y-axis		*Marker pose*	0 °	0.04 °	0.14 °
			Point-to-point	0.04 °	0.36 °	1.12 °
			Point cloud	0.03 °	2.05 °	5.4 °
	Rotation over Z-axis		*Marker pose*	0.01 °	0.33 °	2.79 °
			Point-to-point	0.01 °	1.18 °	4.61 °
			Point cloud	0.02 °	0.61 °	1.76 °
Image-to-patient registration - With reference marker	Euclidean distance	Precision	*Marker pose*	0.55 mm	1.63 mm	4.19 mm
			Point-to-point	0.63 mm	2.7 mm	9.28 mm
			Point cloud	1.19 mm	8.29 mm	73.6 mm
	Rotation over X-axis		*Marker pose*	0.01 °	0.13 °	0.96 °
			Point-to-point	0.02 °	1.5 °	4.94 °
			Point cloud	0.09 °	2.53 °	7.26 °
	Rotation over Y-axis		*Marker pose*	0 °	0.15 °	0.51 °
			Point-to-point	0.01 °	0.33 °	1.17 °
			Point cloud	0.12 °	3.73 °	8.45 °
	Rotation over Z-axis		*Marker pose*	0.01 °	0.28 °	0.9 °
			Point-to-point	0 °	0.95 °	3.24 °
			Point cloud	0.07 °	4.72 °	19.81 °
Implant navigation - Tight-fit	Navigation error (X/Y - plane)	Accuracy	*Tight-fit - Marker pose*	0 mm	2 mm	4 mm
			Tight-fit - Point-to-point	0 mm	3 mm	7 mm
			Tight-fit - Point cloud	0 mm	4 mm	8 mm
	Navigation error (Depth)	Accuracy	*Tight-fit - Marker pose*	0 mm	0 mm	2 mm
			Tight-fit - Point-to-point	0 mm	1 mm	6 mm
			Tight-fit - Point cloud	0 mm	0 mm	6 mm
Implant navigation - No-fit			*No fit - Navigated*	0.51 mm	3.14 mm	7.01 mm
			No fit - Not navigated	0.95 mm	2.5 mm	3.64 mm
Custom coordinate anchor	Euclidean distance	Precision	*Stationary user perspective*	0.28 mm	1.97 mm	5.46 mm
			Dynamic user perspective	3.57 mm	6.75 mm	12.19 mm

5.Discussion

Optimizing patient-specific canine hip implant positioning remains a challenge, and this study investigated the potential of applying a Hololens navigation system (Holoma) for intra-operative AR navigation to increase implant placement accuracy and precision. However, due to the accumulation of technical errors and the challenges faced during the experiments, Holoma could not demonstrate a sufficient accuracy and precision to enhance canine patient-specific hip implant positioning. The current mean placement error of 5 mm was unlikely to be reduced to a maximum of 2-3 mm in real clinical cases by introducing Holoma as intra-operative AR navigation system.

ArUco marker localization and calibration

As the distance between a marker and the camera increased, so did the localization error and uncertainty. Additionally, the amount of light illuminating the ArUco markers determined whether the distance between two markers was underestimated or overestimated.

The observed increase in localization errors with marker-to-camera distances was directly linked to the camera's resolution. The resolution determines the number of pixels that define an image. As markers were positioned farther away from the camera, the number of pixels describing the marker decreased. A lower pixel count resulted in higher inaccuracy and uncertainty in marker detection.

Similar conclusions were drawn by Thabit et al., who also conducted research on the 3D localization error of ArUco markers (33). They tested the effect of different resolutions, marker sizes, and marker-to-camera distances, finding a comparable mean translation error of 2.9±2,0 mm with a resolution of 1920x1080, a marker size of 6x6cm, and a marker-to-camera distance of 50 cm. Smaller translational errors were associated with higher resolutions, larger marker sizes, and shorter distances.

Nunes et al. investigated the accuracy and precision of two calibration setups in the Hololens 1 (34). They also observed an increase in calibration errors with increasing marker-to-camera distances. Despite their experiments being conducted in a warehouse with distances and errors on the scale of meters, a similar effect of distances on the calibration accuracy was observed in our experiments.

The discrepancy in positive and negative measurement errors when comparing normal lighting conditions with overhead surgical lights illuminating the markers, was attributed to inaccuracies in estimating the marker-to-camera distances. Positive measurement errors indicated an overestimation of the distance between two markers. It was suggested that black parts of the markers might have been perceived as white, due to the marker's reflectivity. This phenomenon caused an underestimation of the marker's size and, consequently, an overestimation of the marker-to-camera distance. The amount of light thus influenced the detectability of the markers' edges.

A difficulty in our calibration experiments was the fact that the ArUco markers were undetectable by Holoma when overhead surgical lights were pointed directly on the markers. To estimate the effect of brighter environments, the lights were aimed to illuminate the markers as much as possible, while still being detectable by Holoma.

Marker and pointer tracking

The results of the stationary marker tracking experiments suggested that accurate marker tracking heavily relies on the stability of the Hololens camera. The increased jittering in marker localization during camera movement was likely attributed to the camera's motion blur, software delay, and the Hololens' inability to maintain its virtual coordinate system fixed in the real world (as described in the technical background). The metal ArUco markers appeared to be the most precise in stationary conditions, but camera movement notably affected the precision in this material.
Thabit et al. conducted similar experiments to assess the accuracy of the Hololens in tracking ArUco markers. They also determined the tracking stability in terms of jittering, which they defined as the standard deviation of falsely detected marker movement in mm over a number of frames (33). They concluded translational errors of 0.9 mm for a stationary 6x6 cm ArUco marker, at 100cm from the Hololens' camera. This result closely aligns with our tracking stability of a stationary ArUco marker, suggesting that an uncertainty of almost 1 mm should always be considered when using the Hololens (not only in Holoma) as a navigational instrument due to jittering.

The additional error caused by the registration pointer's arm of 120.5 mm is the direct consequence of the error in ArUco marker orientation estimation, given that the pointer's tip is perpendicular to the ArUco marker's surface. This highlights the necessity not only for continuous accurate ArUco marker position estimation, but also for accurate orientation calculations. To illustrate the impact of miscalculations in the marker's orientation calculations, a misinterpretation of 1° in any direction would lead to a displacement of the pointer's tip with 2.1 mm, according to the law of cosines (35).

The results from the Brainlab tracking experiments confirmed their promised translational error margin of <=2,0 mm (30). However, it is worth mentioning that the Brainlab pointer tracking system is intended for use with a stationary camera. Nonetheless, the experiments in our study suggest that pointer tracking precision may not be substantially affected if the camera would (unintentionally) be moved, as long as the pointer and reference object remain within the camera's field of view.

A major limitation in these experiments is the fact that the gathered data is based on all detected ArUco marker positions, without taking Holoma's detection confidence into account. Holoma can determine the detection confidence, based on the camera stability, viewing angle, and distance between an ArUco marker and the camera. This confidence level would determine whether the localization of a detected marker should be accepted as a reliable measurement. The results of the currently performed experiments therefore don't truthfully represent the marker tracking accuracies of Holoma. The experiments that were impacted the most by these limitations were the ones where movement of the camera is one of the error contributors.

An attempt was made to assess the effect of overhead surgical lights on the detection accuracy and precision of the ArUco markers (made of different materials). Unfortunately, no markers were detected when surgical lights directly illuminated the marker, due to its high reflectivity. Consequently, the results from the dynamic scenarios were deemed unreliable and excluded from the analysis, as the markers were not detected for a substantial portion of the experiments. Appendix B illustrates Hololens' camera perspective when observing three markers of different materials with direct surgical lights illuminating them. This phenomenon poses a major challenge for potential clinical

implementation since most – if not all – surgeries are performed with overhead surgical lights directly illuminating the surgical field. Addressing this issue requires the consideration of solutions such as different materials, additional fiducials, or alternative forms of marker detection.

Coordinate system

Holoma's coordinate system anchor encountered difficulties in maintaining a coordinate system fixed when marker pose registration was performed from five different viewing positions. The assessed accuracy and precision in both stationary and dynamic experiments could be attributed to current coordinate system anchor essentially being a larger version of a standard ArUco marker. The localization errors and jittering quantified in the 'Marker and pointer tracking' experiments were also applicable to the coordinate system anchor, leading to unreliability due to inaccurate and unstable marker detection. Moreover, the dynamic experiments likely introduced an additional error due to the effect of underestimating or overestimating the distance between a marker and the camera, as mentioned in the 'Calibration' experiments. While observing the coordinate system anchor from various directions, Holoma altered the estimated position of the anchor, caused by consistently under- or overestimating the marker-to-camera distances. Consequently, the position and orientation of the registered object changed for each user perspective relative to the coordinate system anchor. Apparently, the effect of the over- or underestimation of the marker-to-camera distance differed for the 35x35mm registration marker compared to the 70x70mm anchor marker.

Vassallo et al. conducted similar experiments to determine the accuracy and precision of Hololens' coordinate system, without the use of an additional coordinate system anchor (36). They positioned a hologram on the same location and extracted its 3D coordinates after participants performed specific movements. Their findings indicated a mean positional variation of a hologram of 5.83 ± 0.51 mm, measured on Hololens' built-in coordinate system. This suggests that an error of approximately 6 mm should always be considered if a participant is expected to move around when the Hololens is used as navigation device, and no coordinate system anchor is incorporated. However, a limitation of their research was the lack of a control measurement, where participants remained stationary in between hologram positionings.

A limitation in Holoma's coordinate system anchor was that Holoma still relied on the Hololens' coordinate system to function properly, as Holoma did not establish its own coordinate system. An example of a strategy to maintain a stationary coordinate system was presented by Brainlab's navigation system. Their registration pointer was continuously tracked relative to the position of a so called 'reference star', but this references star served as the origin for a custom coordinate system, having a known shape and size, and was fixed at a stationary position in the operation room. This allowed the system to operate without depending on an external coordinate system. As long as both objects were in the field of view of the camera, the location of the registration pointer was accurately determined relative to the position of the reference star.

Registration methods

The results of the registration precision and accuracy experiments indicated that marker pose registration yielded the highest precision, followed by point-to-point registration, while point cloud registration was the least precise and accurate registration method. It is important to acknowledge that these results were based on laboratory setting, with well-

defined and distinctive point-to-point and point cloud registration features on the 3D printed object. Real-world clinical cases may be more challenging, as registration points and surfaces will not be as distinctive, probably resulting in decreased registration precision and accuracy.

Unfortunately, the accuracy calculations proved unreliable, due to insufficient precision in marker pose registrations, making it unsuitable as proper control measurement. The registration error of the marker pose registration was most likely associated with the errors originating in stationary marker detection and the coordinate system instability. Additional errors in point-to-point and point cloud registrations were likely caused by errors associated with the localization and tracking of the registration pointer. Point-to-point registration demonstrated slightly better precision than point cloud registrations, potentially because of the reproducibility in the point-to-point locations on the 3D printed object. Differences in rotational variations along the x- and y-axes between point-to-point and point cloud registration could be attributed to the amount of data points, locations of data points, and the distances between the datapoints in x- and y- direction.
The incorporation of a patient reference marker aimed to keep track of patient movement during and after registration, allowing synchronization between the virtual model and the real-world patient. Although our experiments were performed on a stationary object, the addition of a reference marker drastically increased localization errors in the point cloud registrations. The reference marker got frequently occluded by the user's hand and the registration point, which caused a disturbance in the coordinate stability. Effective integration of a patient reference marker requires continuous visibility to the Hololens.

In a literature review by Andrews et al. a variety of image-to-patient registration methods in AR devices were explored (37). They compiled accuracies from manual registration, where a user manually aligns a virtual hologram with its real-world counterpart, and registrations assisted by computer vision or external tracking system. Manual registrations, computer vision assisted registrations, and external tracking system assisted registrations yielded mean distance errors ranging from 1,92 mm to 5,76 mm (38-40), 1,29 mm to 5,20 mm (41-47), and 1,98 mm to 4,03 mm (48, 49), respectively. Given that Holoma's registration methods were computer vision-based, the obtained registration errors were within the mid to high deviation range when compared to other computer vision-based registration methods.

Our experiments directly calculated the registration accuracies and precision, in contrast to the conducted experiments described in Andrews et al.'s review, which indirectly determined registration accuracies. In their experiments, the accuracy of a registration methods was determined based on the accuracy of a performed task that relied on the preceded registration method. However, this approach heavily depended on the ability of a participant to perform a task with high accuracy. In our methods, we aimed to eliminate user-induced errors to calculate the true precision and accuracy of the different registration methods.

Navigation experiments
The results obtained by the tight-fit navigation experiments indicated a correlation between the discrepancy of an ideally positioned implant and the navigation instructions from Holoma, with the registration method. The observed increase in navigation errors across the three registration methods showed a similar trend as the precision results

derived from the registration experiments. The differences between each registration method's precision and the navigation experiments were attributed to user-induced errors and inaccuracies in virtualizing the implant with its attached ArUco marker.
Using CBCT, the implant and its attached ArUco marker were virtually reconstructed. This process involved manual determination of the ArUco marker's center and plane to accurately recreate the 3D relationship between the marker and the implant. However, the tight-fit navigation results revealed a systematic error of 2 mm, likely caused by an inaccurate virtualization of the implant. The manual recreation of an exact virtual relation between the marker and the implant proved to be challenging.
The precision of the tight-fit navigation experiments was notably affected by random errors, caused by the instability of the detected ArUco markers. At times, Holoma would unexpectedly shift its navigation instructions by a few millimeters, even when both the implant and the participant remained stationary.
The presence of systematic and random errors induced by the implant navigation attachment became apparent in the no-fit navigation tests, as both accuracy an precision improved without the use of active navigation. A comparison between the not-navigated and the navigated no-fit experiments revealed a decrease in both median error and its range (excluding the single outlier), suggesting an increase in accuracy and precision. This experiment was also performed to assess feasibility of AR navigation, purely based on visual guidance. Our findings suggested that this approach, in laboratory setting, was not inferior to an active navigation approach, and that an implant could be consistently positioned within an error margin of 4 mm.

The evaluation of user-induced error in implant navigation involved a direct comparison between the tight-fit marker pose navigation and the navigated no-fit navigation experiments. The increase in placement errors when comparing these particular experiments, was attributed to the user's interpretation and execution of Holoma's navigation instructions. This observation was similar with the findings of Meulstee et al., who conducted research involving tight-fit and loose-fit experiments with a conventional image-guided system (IGS) (Brainlab) and compared it with the addition of AR visualization (50). They found a significant difference in implant placement errors between conventional IGS and AR assisted placement in the loose-fit experiments (0.7mm ± 0.4mm vs 2.3mm ± 0.5mm, $P<0.001$), but not in the tight-fit experiments (0.6mm ± 0.2mm vs 0.7mm ± 0.2mm, $P =0.99$). This suggested that the main cause for the inaccuracies in their AR navigation was not the performance of the navigation software itself, but the user's interpretation and the model visualization. Their obtained difference between the AR guided tight-fit navigation and loose-fit navigation tests aligned with our own findings.
García-Sevilla et al. conducted research on AR guided patient specific pelvic instrument placement and concluded a median placement error of 1,84 mm (*min; max:* 0,51; 4,13), compared to a median placement error of 3,37 mm (0,41; 54,03) in freehand placement (51). Their results indicated a potential remarkable improvement of pelvic implant positioning when applying AR navigation.

One limitation was a major software update after two of the four participants had already performed the tight-navigation experiments. The results of the older software version were excluded from analyses, because a software bug had been fixed in the meantime.

Future research

Future research should focus on alternative strategies to increase implant positioning.
Meulstee et al. already revealed a maximum simplified implant positioning error of 2.9 mm was achievable, when combining the Hololens with Brainlab's navigation system (50). The combination of optical tracking devices with AR visualization could be the future of AR navigation applications.
Head mounted displays other than the Hololens should be considered as well. Kivovics et al. determined mean implant positioning error of 1.27 mm and 1.34 mm by utilizing the Magic Leap one for AR based navigation in dental surgery (52).
Other techniques such as robot assisted surgery were investigated to improve total knee arthroplasty accuracy and precision, and showed promising results (53-55). One recent study was already applied robotic assisted surgery for a patient specific implant in a sheep model, and a mean implant positioning error of 1.05 ± 0.53 mm was achieved (56).

Future research with Holoma might focus on exploring the possibilities to utilize Holoma for training and instruction purposes. While the current achievable accuracies might not be good enough to improve the hip implant positioning, it could be a great tool to introduce existing and new techniques to third parties. A demonstration (e.g. on phantom bones) of the relatively novel canine hip implant procedure would become more valuable, if the participants could observe the limitations of the surgical procedure and the correct position of the implant.
Holoma is also constantly improving and adjusting their software capabilities and therefore improving navigation accuracies. Future research could keep track of their improvements and compare the improvements with the acquired data from this study. If improvements reaches accuracies and precision within margin of 3 millimeters in real clinical scenarios, Holoma might be able to enhance implant positioning.

6.Conclusion

In conclusion, Holoma is able to navigate implant placements in laboratory setting within a range of 4 to 8 mm, depending on the registration method applied. The accuracy and precision of the navigation software were determined to be inadequate to decrease patient specific hip implant placement errors, at the time of investigating. Future improvements of Holoma's accuracies will determine its suitability as an intra-operative AR based navigation system. In the meantime, alternative strategies should be considered and investigated to increase implant placement accuracies.

7.References

1. Normal Hip X-rays: Radiopaedia; [Available from: https://radiopaedia.org/cases/normal-hip-x-rays
2. Modern approach to developmental dysplasia of the hip: Mayoclinic; [Available from: https://www.mayoclinic.org/medical-professionals/pediatrics/news/modern-approach-to-developmental-dysplasia-of-the-hip/mac-20538657#dialogId61600004
3. Nandhagopal T, De Cicco FL. Developmental dysplasia of the hip. StatPearls [Internet]: StatPearls Publishing; 2022.
4. Loder RT, Skopelja EN. The epidemiology and demographics of hip dysplasia. ISRN Orthop. 2011;2011:238607.
5. Upasani VV, Bomar JD, Matheney TH, Sankar WN, Mulpuri K, Price CT, et al. Evaluation of brace treatment for infant hip dislocation in a prospective cohort: defining the success rate and variables associated with failure. JBJS. 2016;98(14):1215-21.
6. Atalar H, Sayli U, Yavuz O, Uraş I, Dogruel H. Indicators of successful use of the Pavlik harness in infants with developmental dysplasia of the hip. International Orthopaedics. 2007;31:145-50.
7. Dwan K, Kirkham J, Paton RW, Morley E, Newton AW, Perry DC. Splinting for the non-operative management of developmental dysplasia of the hip (DDH) in children under six months of age. Cochrane Database of Systematic Reviews. 2022(10).
8. Bittersohl B, Hosalkar HS, Wenger DR. Surgical treatment of hip dysplasia in children and adolescents. Orthopedic Clinics. 2012;43(3):301-15.
9. Pemberton PA. Pericapsular osteotomy of the ilium for treatment of congenital subluxation and dislocation of the hip. JBJS. 1965;47(1):65-86.
10. Ganz R, Klaue K, Vinh TS, Mast JW. A New Periacetabular Osteotomy for the Treatment of Hip Dysplasias Technique and Preliminary Results. Clinical Orthopaedics and Related Research (1976-2007). 1988;232:26-36.
11. Chiari K. Medial displacement osteotomy of the pelvis. Clinical Orthopaedics and Related Research (1976-2007). 1974;98:55-71.
12. Staheli LT. Slotted acetabular augmentation. Journal of Pediatric Orthopaedics. 1981;1(3):321-7.
13. Ezirmik N, Yildiz K. A study on the complications of surgical treatment for bilateral developmental dysplasia of the hip and a comparison of two osteotomy techniques. Eurasian J Med. 2011;43(3):162-8.
14. Willemsen K, Möring MM, Harlianto NI, Tryfonidou MA, van der Wal BC, Weinans H, et al. Comparing hip dysplasia in dogs and humans: A review. Frontiers in veterinary science. 2021;8:791434.
15. Rettenmaier JL, Keller GG, Lattimer JC, Corley EA, Ellersieck MR. Prevalence of canine hip dysplasia in a veterinary teaching hospital population. Vet Radiol Ultrasound. 2002;43(4):313-8.
16. Willemsen K, Tryfonidou M, Sakkers R, Castelein RM, Zadpoor AA, Seevinck P, et al. Patient-specific 3D-printed shelf implant for the treatment of hip dysplasia: Anatomical and biomechanical outcomes in a canine model. Journal of Orthopaedic Research®. 2022;40(5):1154-62.
17. Willemsen K, Tryfonidou MA, Sakkers RJ, Castelein RM, Beukers M, Seevinck PR, et al. Patient-specific 3D-printed shelf implant for the treatment of hip dysplasia tested in an experimental animal pilot in canines. Scientific Reports. 2022;12(1):3032.
18. Kwananocha I, Magré J, Willemsen K, Weinans H, Sakkers RJ, How T, et al. Acetabular rim extension using a personalized titanium implant for treatment of hip dysplasia in dogs: short-term results. Frontiers in Veterinary Science. 2023;10:1160177.
19. Bosma SE, Wong KC, Paul L, Gerbers JG, Jutte PC. A Cadaveric Comparative Study on the Surgical Accuracy of Freehand, Computer Navigation, and Patient-Specific Instruments in Joint-Preserving Bone Tumor Resections. Sarcoma. 2018;2018:4065846.

20. Evrard R, Schubert T, Paul L, Docquier PL. Quality of resection margin with patient specific instrument for bone tumor resection. J Bone Oncol. 2022;34.
21. Garcia-Sevilla M, Mediavilla-Santos L, Ruiz-Alba MT, Perez-Mananes R, Calvo-Haro JA, Pascau J. Patient-specific desktop 3D-printed guides for pelvic tumour resection surgery: a precision study on cadavers. Int j comput assist radiol surg. 2021;16(3):397-406.
22. Garcia-Sevilla M, Moreta-Martinez R, Garcia-Mato D, Pose-Diez-de-la-Lastra A, Perez-Mananes R, Calvo-Haro JA, et al. Augmented Reality as a Tool to Guide PSI Placement in Pelvic Tumor Resections. Sensors (Basel). 2021;21(23).
23. Khan FA, Lipman JD, Pearle AD, Boland PJ, Healey JH. Surgical technique: Computer-generated custom jigs improve accuracy of wide resection of bone tumors. Clin Orthop Relat Res. 2013;471(6):2007-16.
24. Park JW, Kang HG, Lim KM, Park DW, Kim JH, Kim HS. Bone tumor resection guide using three-dimensional printing for limb salvage surgery. J Surg Oncol. 2018;118(6):898-905.
25. Sallent A, Vicente M, Reverte MM, Lopez A, Rodriguez-Baeza A, Perez-Dominguez M, et al. How 3D patient-specific instruments improve accuracy of pelvic bone tumour resection in a cadaveric study. Bone Joint Res. 2017;6(10):577-83.
26. Wong K-C, Sze K-Y, Wong IO-L, Wong C-M, Kumta S-M. Patient-specific instrument can achieve same accuracy with less resection time than navigation assistance in periacetabular pelvic tumor surgery: a cadaveric study. International Journal of Computer Assisted Radiology and Surgery. 2016;11(2):307-16.
27. Wong KC, Kumta SM, Geel NV, Demol J. One-step reconstruction with a 3D-printed, biomechanically evaluated custom implant after complex pelvic tumor resection. Comput Aided Surg. 2015;20(1):14-23.
28. Matthews JH, Shields JS. The Clinical Application of Augmented Reality in Orthopaedics: Where Do We Stand? Curr Rev Musculoskelet Med. 2021;14(5):316-9.
29. AG B. The Brainlab Companies [Website]. 2023 [Available from: https://www.brainlab.com/.
30. BrainLab. Software User Guide Rev. 1.7 Cranial/ENT Ver. 3.1. 2023.
31. Microsoft. Spatial mapping in Unity - Mixed Reality [Website]. 2023 [Available from: https://learn.microsoft.com/en-us/windows/mixed-reality/develop/unity/spatial-mapping-in-unity?tabs=mrtk.
32. Microsoft. Coordinate systems 2023 [Available from: https://learn.microsoft.com/en-us/windows/mixed-reality/design/coordinate-systems.
33. Thabit A, Niessen WJ, Wolvius EB, Van Walsum T, editors. Evaluation of marker tracking using mono and stereo vision in Microsoft HoloLens for surgical navigation. Medical Imaging 2022: Image-Guided Procedures, Robotic Interventions, and Modeling; 2022: SPIE.
34. Nunes JS, Almeida FB, Silva LS, Santos VM, Santos AA, de Senna V, et al. Three-dimensional coordinate calibration models for augmented reality applications in indoor industrial environments. Applied Sciences. 2023;13(23):12548.
35. Cosine Theorem: Encyclopedia of Mathematics; [Available from: https://encyclopediaofmath.org/index.php?title=Cosine_theorem.
36. Vassallo R, Rankin A, Chen EC, Peters TM, editors. Hologram stability evaluation for Microsoft HoloLens. Medical Imaging 2017: Image Perception, Observer Performance, and Technology Assessment; 2017: SPIE.
37. Andrews CM, Henry AB, Soriano IM, Southworth MK, Silva JR. Registration techniques for clinical applications of three-dimensional augmented reality devices. IEEE journal of translational engineering in health and medicine. 2020;9:1-14.
38. Frantz T, Jansen B, Duerinck J, Vandemeulebroucke J. Augmenting Microsoft's HoloLens with vuforia tracking for neuronavigation. Healthcare technology letters. 2018;5(5):221-5.
39. Li Y, Chen X, Wang N, Zhang W, Li D, Zhang L, et al. A wearable mixed-reality holographic computer for guiding external ventricular drain insertion at the bedside. Journal of neurosurgery. 2018;131(5):1599-606.

40. McJunkin JL, Jiramongkolchai P, Chung W, Southworth M, Durakovic N, Buchman CA, et al. Development of a mixed reality platform for lateral skull base anatomy. Otology & Neurotology: Official Publication of the American Otological Society, American Neurotology Society [and] European Academy of Otology and Neurotology. 2018;39(10):e1137.
41. Andress S, Johnson A, Unberath M, Winkler AF, Yu K, Fotouhi J, et al. On-the-fly augmented reality for orthopedic surgery using a multimodal fiducial. Journal of Medical Imaging. 2018;5(2):021209-.
42. Condino S, Carbone M, Piazza R, Ferrari M, Ferrari V. Perceptual limits of optical see-through visors for augmented reality guidance of manual tasks. IEEE Transactions on Biomedical Engineering. 2019;67(2):411-9.
43. Condino S, Turini G, Parchi PD, Viglialoro RM, Piolanti N, Gesi M, et al. How to build a patient-specific hybrid simulator for orthopaedic open surgery: benefits and limits of mixed-reality using the Microsoft HoloLens. Journal of healthcare engineering. 2018;2018.
44. Jiang T, Yu D, Wang Y, Zan T, Wang S, Li Q. HoloLens-based vascular localization system: precision evaluation study with a three-dimensional printed model. Journal of medical Internet research. 2020;22(4):e16852.
45. Jiang T, Zhu M, Chai G, Li Q. Precision of a novel craniofacial surgical navigation system based on augmented reality using an occlusal splint as a registration strategy. Scientific reports. 2019;9(1):501.
46. Liu H, Auvinet E, Giles J, Rodriguez y Baena F. Augmented reality based navigation for computer assisted hip resurfacing: a proof of concept study. Annals of biomedical engineering. 2018;46:1595-605.
47. Moreta-Martinez R, García-Mato D, García-Sevilla M, Pérez-Mañanes R, Calvo-Haro J, Pascau J. Augmented reality in computer-assisted interventions based on patient-specific 3D printed reference. Healthcare technology letters. 2018;5(5):162-6.
48. Azimi E, Qian L, Navab N, Kazanzides P. Alignment of the virtual scene to the tracking space of a mixed reality head-mounted display. arXiv preprint arXiv:170305834. 2017.
49. Xvision Spine System (XVS) 510(K) Clearance.
50. Meulstee J, Nijsink H, Schreurs R, Verhamme L, Xi T, Delye H, et al. Toward Holographic-Guided Surgery. Surgical Innovation. 2018;26:155335061879955.
51. García-Sevilla M, Moreta-Martinez R, García-Mato D, Pose-Diez-de-la-Lastra A, Pérez-Mañanes R, Calvo-Haro JA, et al. Augmented reality as a tool to guide PSI placement in pelvic tumor resections. Sensors. 2021;21(23):7824.
52. Kivovics M, Takács A, Pénzes D, Németh O, Mijiritsky E. Accuracy of dental implant placement using augmented reality-based navigation, static computer assisted implant surgery, and the free-hand method: an in vitro study. Journal of Dentistry. 2022;119:104070.
53. Deckey DG, Rosenow CS, Verhey JT, Brinkman JC, Mayfield CK, Clarke HD, et al. Robotic-assisted total knee arthroplasty improves accuracy and precision compared to conventional techniques. The Bone & Joint Journal. 2021;103(6 Supple A):74-80.
54. Doan GW, Courtis RP, Wyss JG, Green EW, Clary CW. Image-free robotic-assisted total knee arthroplasty improves implant alignment accuracy: a cadaveric study. The Journal of Arthroplasty. 2022;37(4):795-801.
55. Vaidya N, Jaysingani TN, Panjwani T, Patil R, Deshpande A, Kesarkar A. Assessment of accuracy of an imageless hand-held robotic-assisted system in component positioning in total knee replacement: a prospective study. Journal of Robotic Surgery. 2022;16(2):361-7.
56. Williamson T, Ryan S, Buehner U, Sweeney Z, Hill D, Lozanovski B, et al. Robot-assisted implantation of additively manufactured patient-specific orthopaedic implants: evaluation in a sheep model. International Journal of Computer Assisted Radiology and Surgery. 2023:1-11.

8. Appendix A

8.1. Registration box design process

Goal: Design a 3D-printable model on which Holoma's three registration methods (Marker pose, Point-to-point, Point cloud) can repeatedly and precisely be performed.

Requirements:

- Groove for an ArUco marker to tightly fit in, so the location of the ArUco marker can be predefined as accurate as possible.
- Locations where the registration pointer can be positioned reproducibly to perform point-to-point registration as precise and accurate as possible.
- Clearly defined surface areas for point cloud registration, where physical boundaries determine the locations where a participant needs to perform 'surface scratching' for precise registration. Also, the areas need to be defined in all three planes of a 3D coordinate system, so no ambiguous orientation is possible. Lastly, the areas need steep curvatures so the virtual model can be easily matched to the physical object.

Final design:

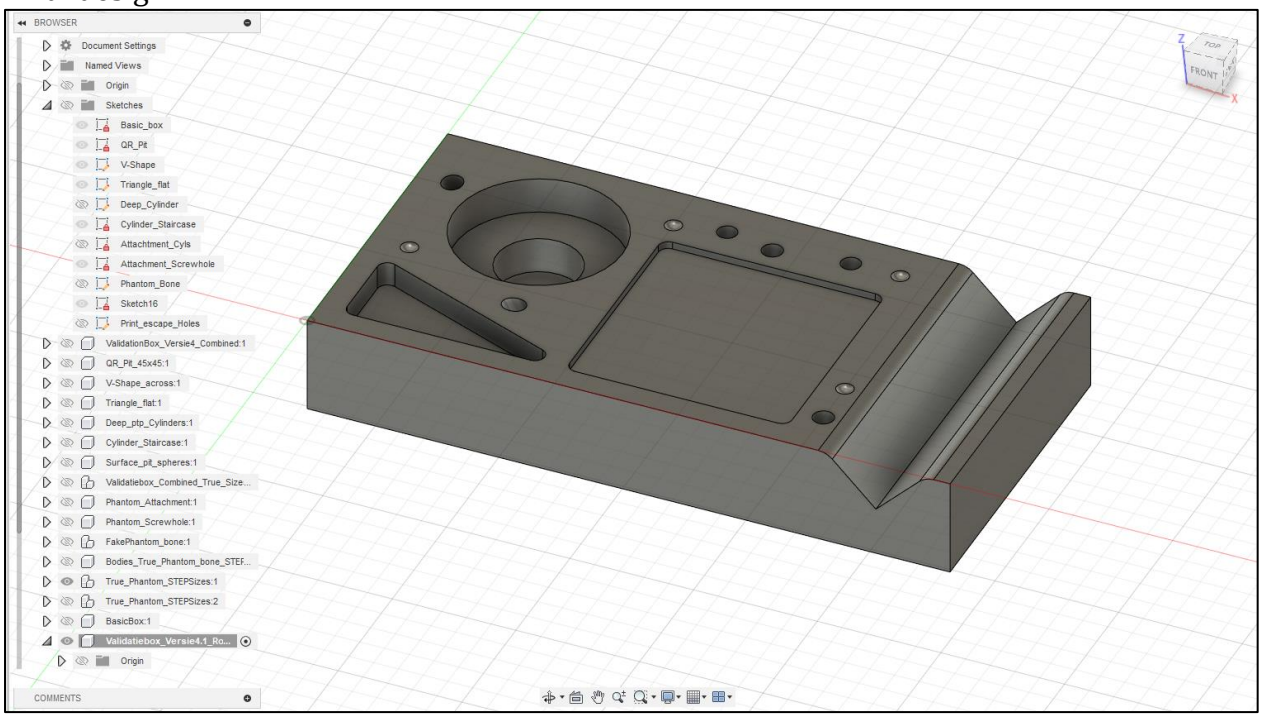

Design process in Fusion 360:
Object is designed in Fusion 360 so .CAD objects can be created, which are more accurate and precise virtual models when compared to .STL object. In the end, the object was 3D printed, but CNC machining was considered as well, so a .CAD design was preferred over .STL files.
The design process consisted of creating the necessary shapes for the three registration methods, while documenting the dimensions and the positions of certain objects. The exact position of the ArUco marker groove and the point-to-point pits were necessary to assure precise virtual model transfer and preplanning to Holoma.

8.1.1. Basic shape

Sketch a rectangle with shape 130x65mm and extrude it with -20mm.

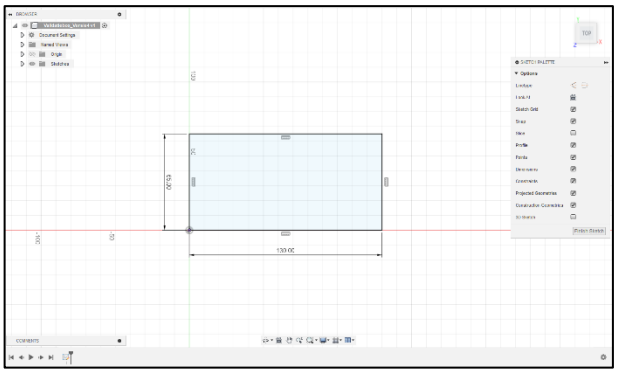

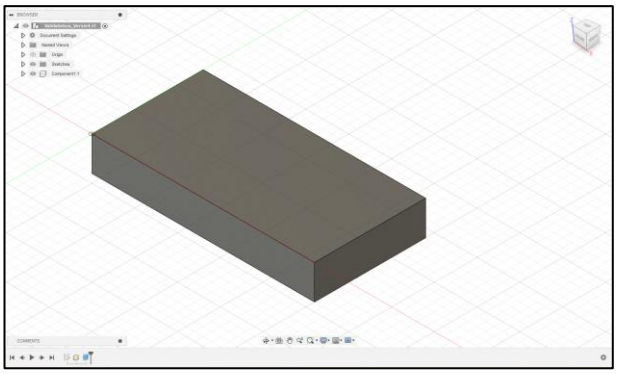

Important coordinates:

- Corner at (0, 0, 0)
- X-, Y-, Z-lenghts = 130x65x20 mm

8.1.2. ArUco marker groove

Create a sketch with a 45x45 mm square (ArUco marker size including white borders), translate it +50 mm over the x-axis, and +5 mm over the y-axis. 'Fillet' the corners with a 2 mm radius. Extrude the sketch with -1.5 mm (height of an ArUco marker).

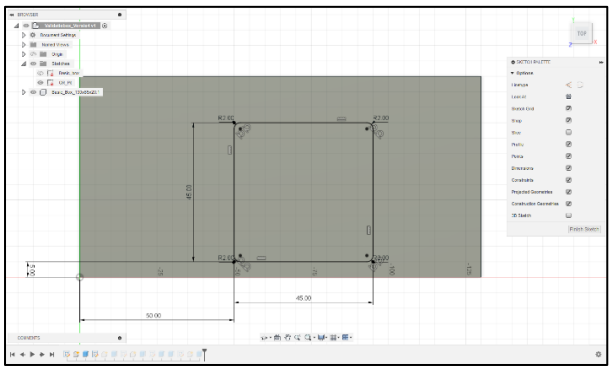

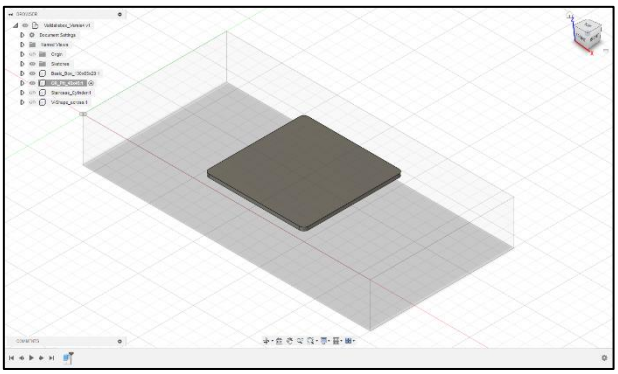

Important coordinates:

- Center of ArUco surface at (72.5; 27.5; 0)

8.1.3. Point cloud registration surfaces

Crossing V-shape

Create a new sketch. Set the ‘front’ face of the 3D rectangle as sketching surface. Draw a triangle, starting 5 mm from the edge, with an angle of 90 degrees, with an height of 10 mm. Extrude the sketch with -65 mm to match the length of the 3D rectangle.

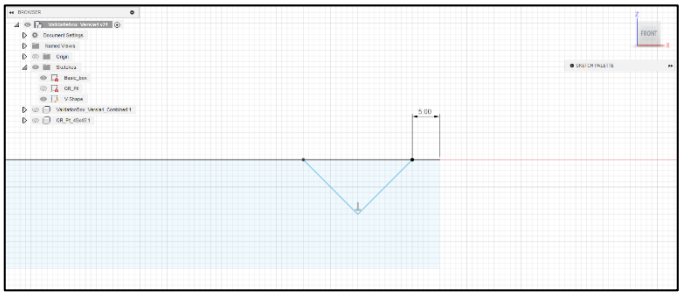

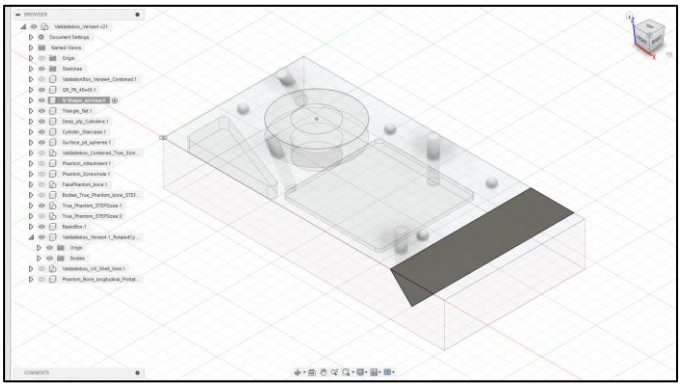

Flat triangle

Create a new sketch with the ‘top’ face of the 3D rectangle as sketching surface. Create a 90 degree angled triangle, translated +5 mm over the x- and y-axes, with a length and

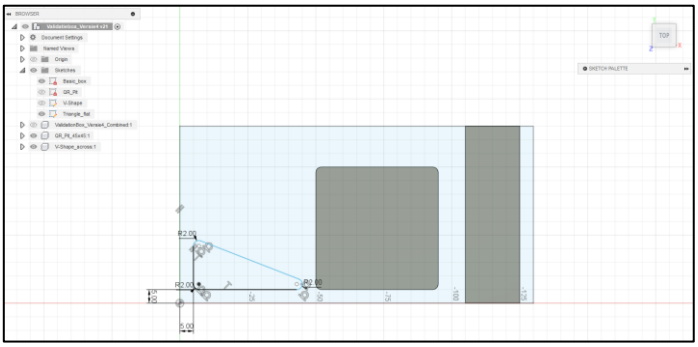

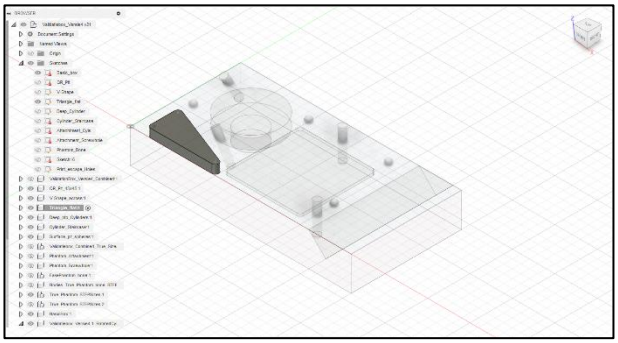

height of 40x18 mm. Fillet the corners with a radius of 2 mm. Extrude with -5 mm.

Staircase cylinders

Create a new sketch. Create a circle with a diameter of 34 mm. Translate it +28 mm over the x-axis, and +22 mm over the y-axis. Create another circle with a diameter of 17 mm, setting the same center as the first circle. Extrude the larger circle with -7.5 mm, and the smaller circle with -15 mm. Join the two (now) cylinders into one component.

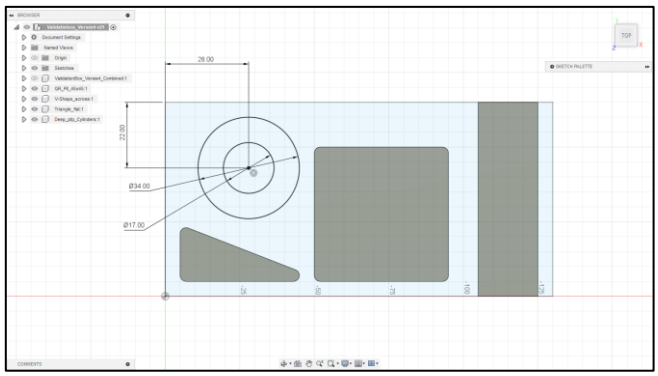

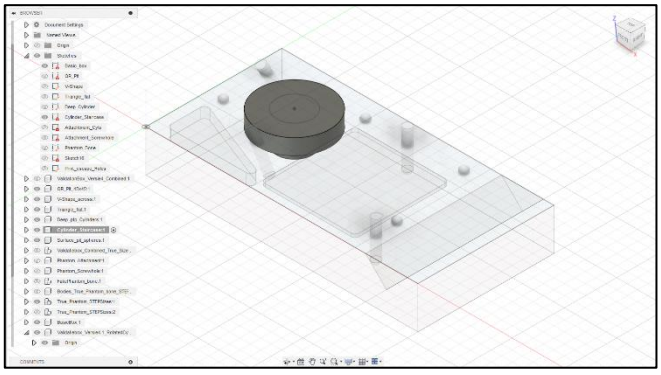

8.1.4. Point-to-point registration

Deep cylindric pits

Create a new sketch and set the z/x-plane as sketching plane. Create a rectangle of 20x2 mm with the left lower corner touching coordinate (0, 0, 0). Fillet the right lower corner with a radius of 2 mm. Resolve the sketch with 360 degrees over the z-axis.

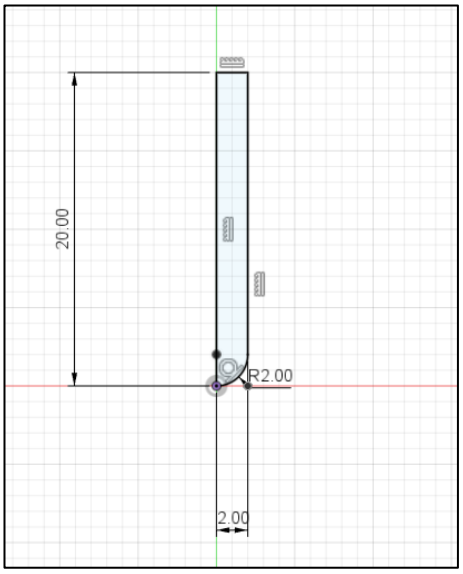

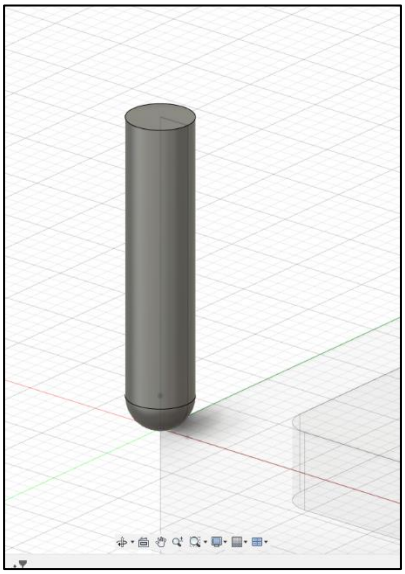

These cylinders are used to create specified locations inside the 3D rectangle which can be reproduced with the real-life registration pointer. Two cylinders remained in a straight orientation, one cylinder was rotated with 30 degrees over the x-axis, one cylinder was rotated with 30 degrees over the y-axis. The four cylinders were translated in three directions, all relative to the coordinate systems origin, according to the values presented in table 6.

Table 6 Translations of the 4 cylinders over the three axes

	Cyl_1	Cyl_2	Cyl_3	Cyl_4
X-axis	7	40	70	100
Y-axis	58	20	55	10
Z-axis	-12	-12	-12	-12

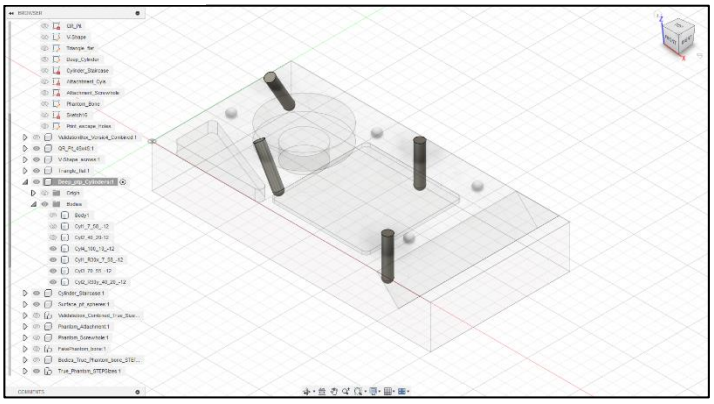

3D coordinates of deep cylindric pits:

- (7, 58, -12)
- (40, 20, -12)
- (70, 55, -12)
- (100, 10, -12)

Surface pits
Create a sphere with a diameter of 4 mm and the origin at (0, 0, 0). Copy the sphere four times, and translate each sphere according to table 7. The registration pointer will touch the 3D rectangular surface inside the pits at -1 mm, since the spheres have a radius of 2 mm, translating the centers with +1 mm over the z-axis.

Table 7 Translations of the 4 spheres over the three axes.

	Sphere_1	Sphere_2	Sphere_3	Sphere_4
X-axis	8	50	95	100
Y-axis	29	55	57	20
Z-axis	1	1	1	1

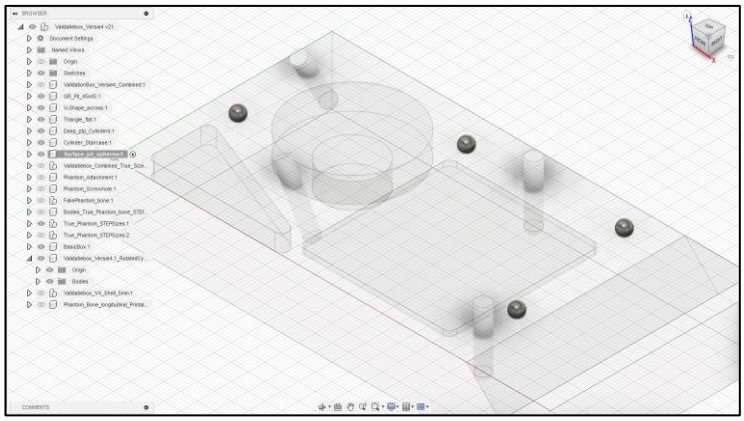

8.1.5. Boolean subtract all components

All components for ArUco marker attachment, point cloud, and point-to-point registration were subtracted from the 3D rectangle. Finally, a fillet with a radius of 4 mm was performed on the edges of the crossing V-shape. The object presented a 'Final design' in the beginning of this Appendix is now created.

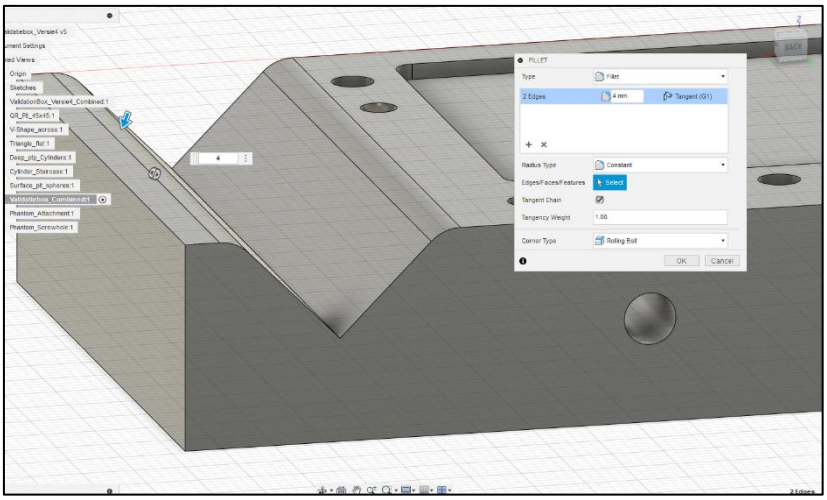

8.1.6. Shell the object

A shell of 5 mm was created out of the 3D object to make 3D printing feasible.

8.2. Phantom bone design process

Goal: To design a simplified phantom bone objects, on which a simplified, circular implant could be positioned with precisely defined implant center positions. The phantom bone needs to be attachable to the 'Registration box' at least in two orientations. One orientation needs to facilitate tight-fit experiments, and the other orientation facilitates the no-fit experiment.

Requirements:

- Multiple locations where a circular simplified implants can be tightly positioned.
- A flat surface where a flat simplified implant can be positioned anywhere.
- A way to tightly attach the phantom bone to the registration box to perform implant navigation after image-to-patient registration.

Final design:

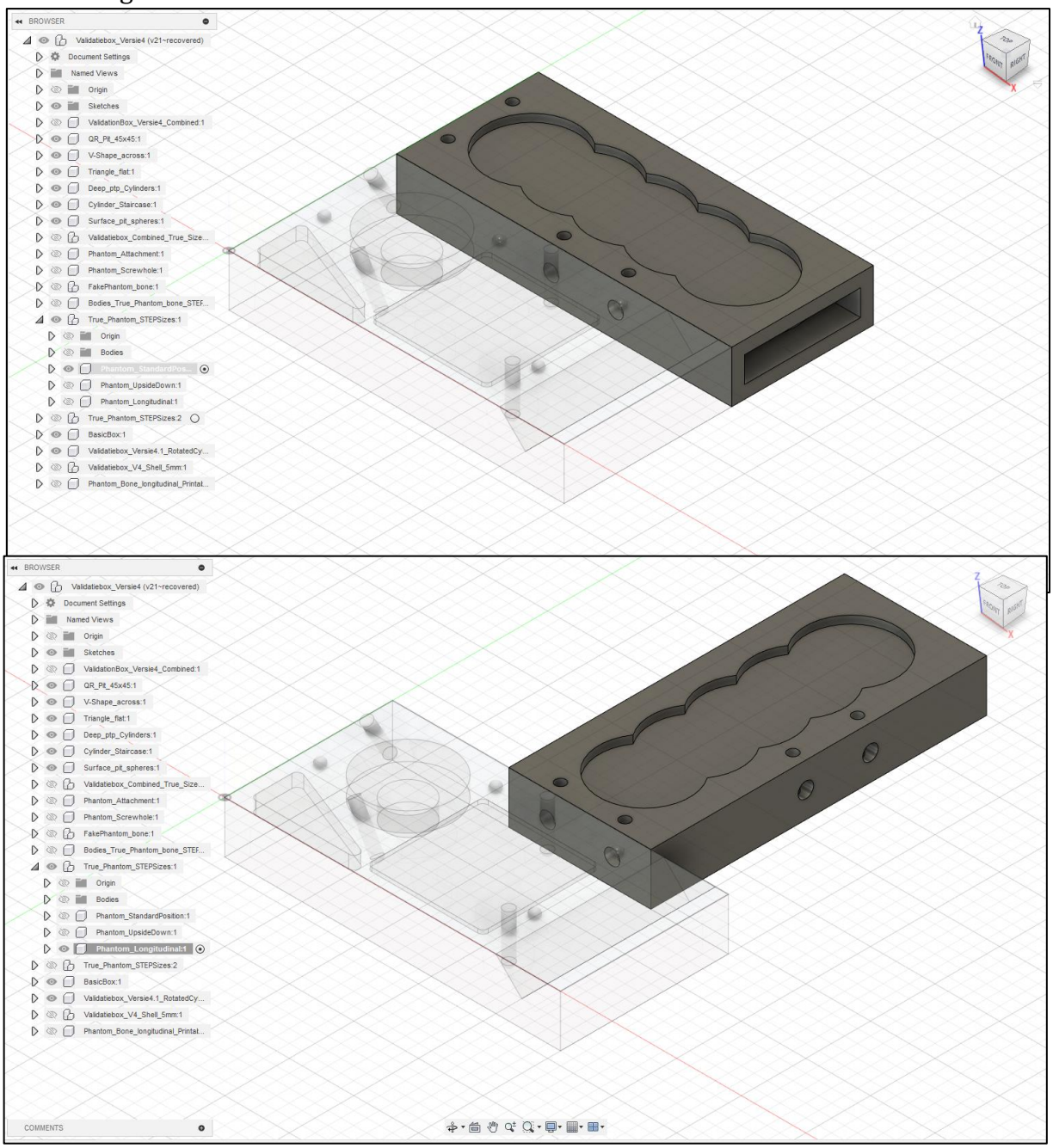

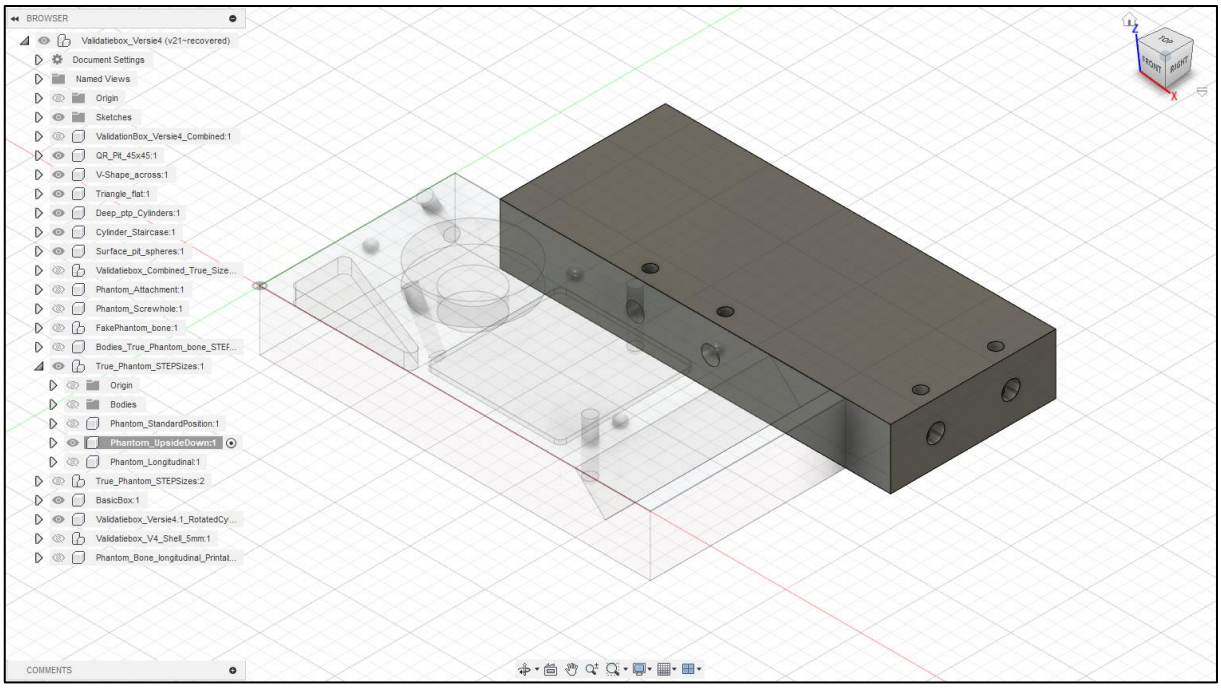

Design process

8.2.1. Basic shape

Create a new sketch. Make a rectangle of size 130x55 mm and extrude is with -20 mm. Translate the entire box with +65 mm over the y-axis.

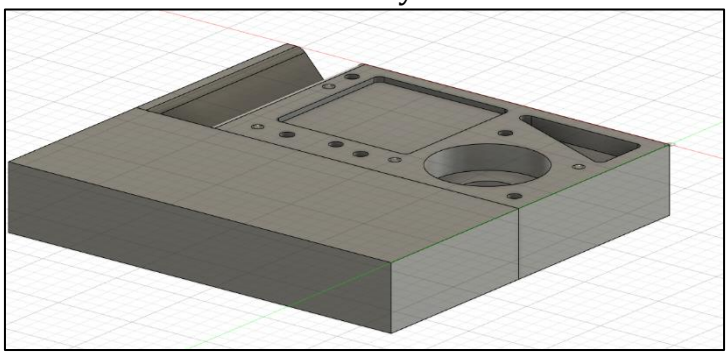

8.2.2. Tight-fit implant positions

Create a new sketch. Make a circle with a diameter of 35 mm and translate it 25 mm over the x-axis, and 92.25 mm over the y-axis. Extrude with -3 mm. Create a rectangular pattern, with five samples over 80 mm. The center coordinates of the implant positions are presented in table 8.

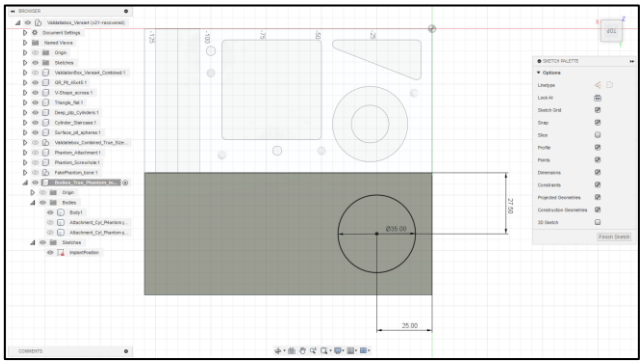

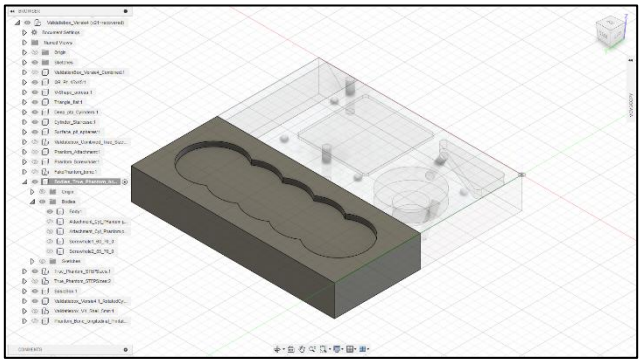

Table 8 3D coordinates of implant center at the surface of the phantom bone (X, Y, Z).

	Implant positions				
	1	*2*	*3*	*4*	*5*
Normal orientation	(25, 92.5, -3)	(45, 92.5, -3)	(65, 92.5, -3)	(85, 92.5, -3)	(105, 92.5, -3)
Longitudinal orientation	(72.5, 90, -3)	(72.5, 110, -3)	(72.5, 130, -3)	(72.5, 150, -3)	(72.5, 170, -3)

8.2.3. Phantom to box attachment

To attach the phantom bone to the registration box, two long cylinders were created and Boolean subtracted from both objects. Above each cylinder, a screw hole was created in both the registration box as well as the phantom bone. When observing from the 'back' face, the center of the cylinders are located on the x-axis at 60 mm and 85 mm from the origin, and on z-axis at -10 mm from the origin.

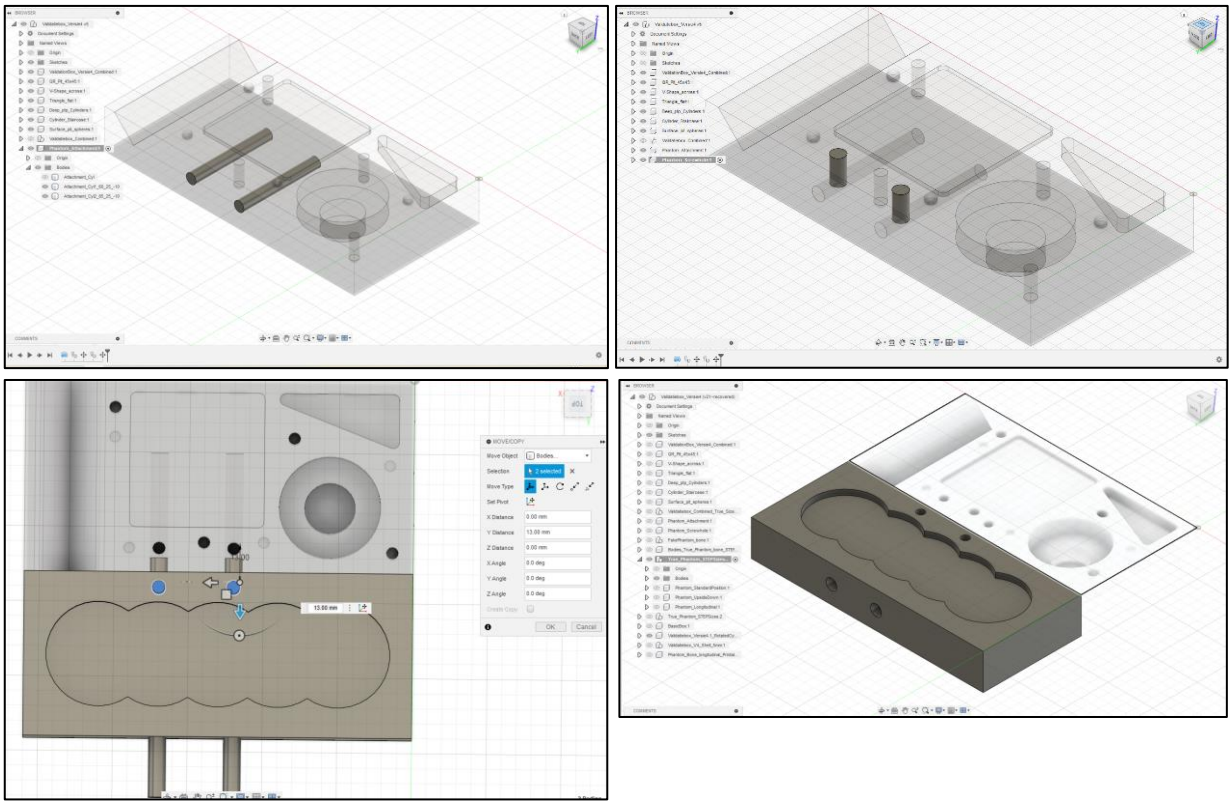

8.2.4. Longitudinal phantom bone

The phantom bone is rotated with 90 degrees over the z-axis and the center of its face is located in the middle between the two attachment cylinders. The same cylinders are Boolean subtracted from the new oriented phantom bone with two screwholes above it. The 3D coordinates of the five implant positions are presented in table 7.

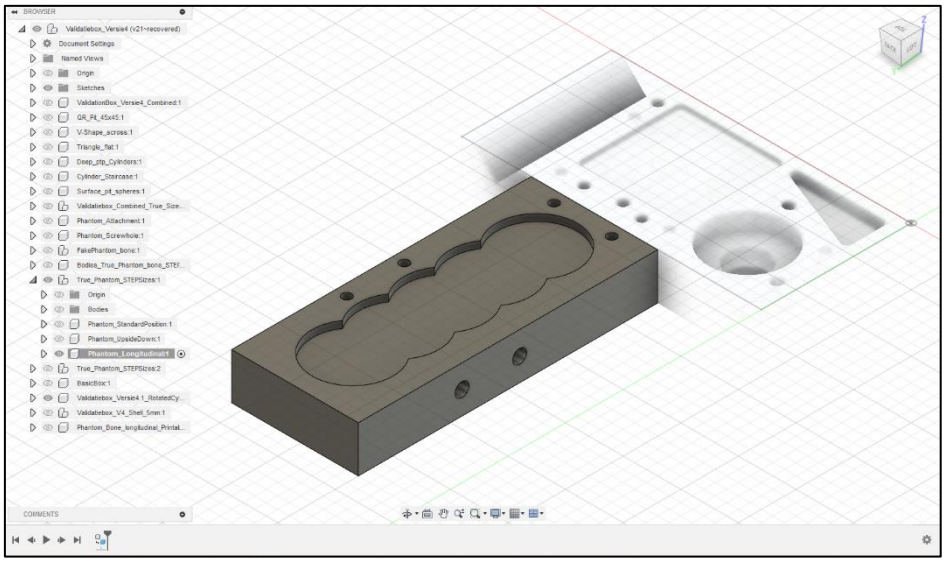

8.2.5. Flat surface phantom bone.

The other side of the phantom is flat, so the bone is rotated with 90 degrees over the x-axis and the attachment cylinders are aligned accordingly.

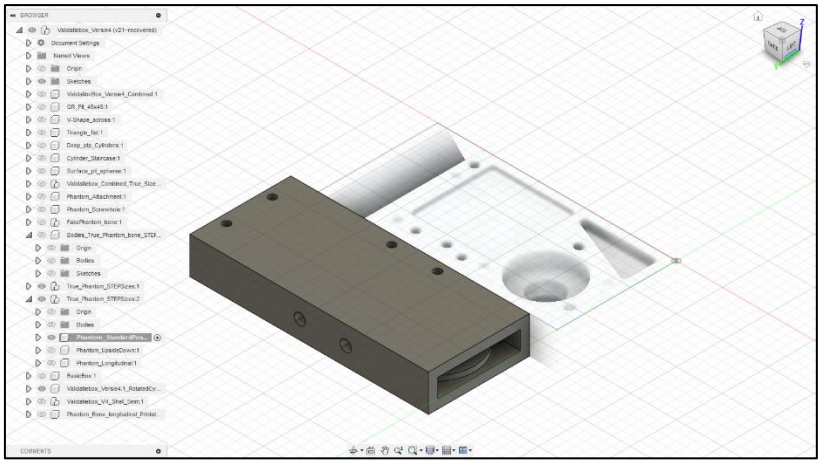

8.2.6. Shell the object

A shell of 5 mm was created out of the 3D object to make 3D printing feasible.

Object export

Both the registration box and the phantom bone were saved as .CAD files.

8.2.7. Simplified circular implant

The implant was a simple circle with a height of 3 mm. To attach the implant to an ArUco marker, a previously designed object was used. The original design aimed to attach an ArUco marker to a real implant. The real implant was changed with a simple 3D circle.
The screwed object from the original design was subtracted from the 3D circle. A fillet of 1 mm was applied on the edges of the circle. The circle was exported as .STL file.

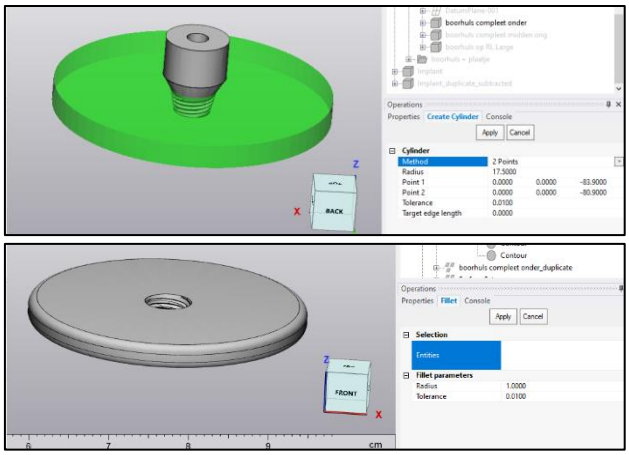

8.3. 3-Matic case preparations

The implant positions needed to be created in 3-Matic as instrument end positions. The .CAD files were imported as .STL files with a surface accuracy of 0.01. For both the normal oriented as well as the longitudinal oriented tight-fit experiments, axes are created on the predefined implant positions (as described in table 8). The axes should end exactly at the phantom surface. During implant navigation, Holoma will then instruct the user to stop movements when the implant surface touches the phantom surface.

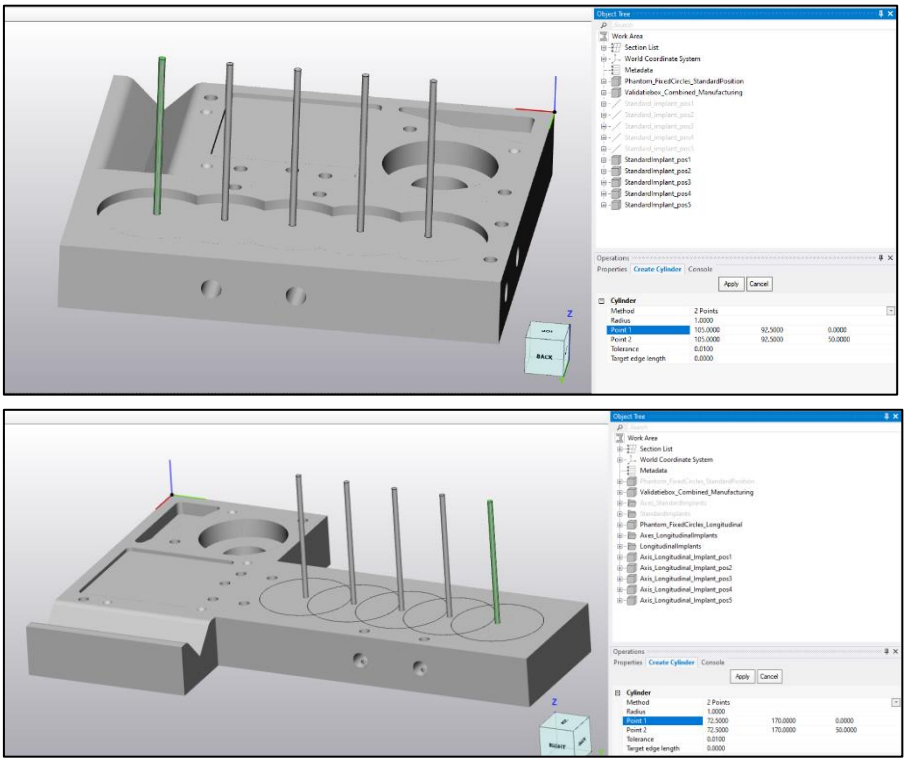

Also, virtual implant models are created so they can be visualized inside Holoma.

For the no-fit experiments, implant positions need to be determined on the flat phantom bone surface. The three positions were chosen on the following 3D coordinates, and corresponding axes were created:

- (40, 93, 0)
- (80, 102, 0)
- (118, 83, 0)

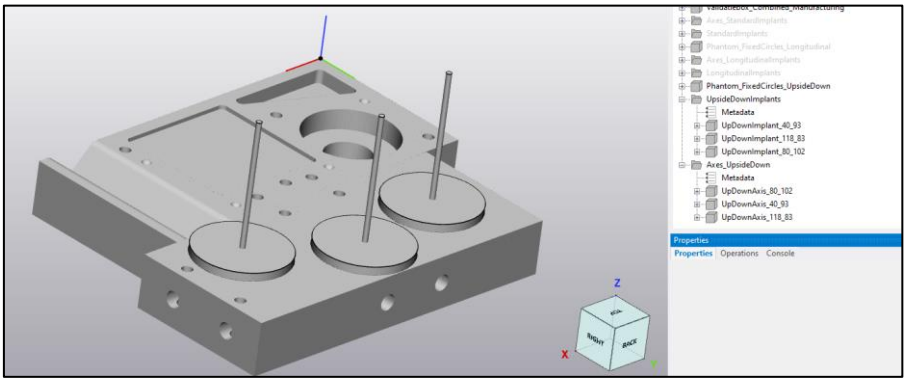

Object extraction

The instrument axes and implants were exported and saved as .STL files for further processing.

8.4. Blender model preparations

Final preparations need to be performed in Blender, a free-to-use 3D modelling software. The objects can be exported as .GLB's, which is the primary file type used in AR visualization. The registration box, phantom bone(s), implant positions, marker pose registration marker position, point-to-point registration locations, and point cloud registration areas need to be defined in Blender and exported as .GLB files.

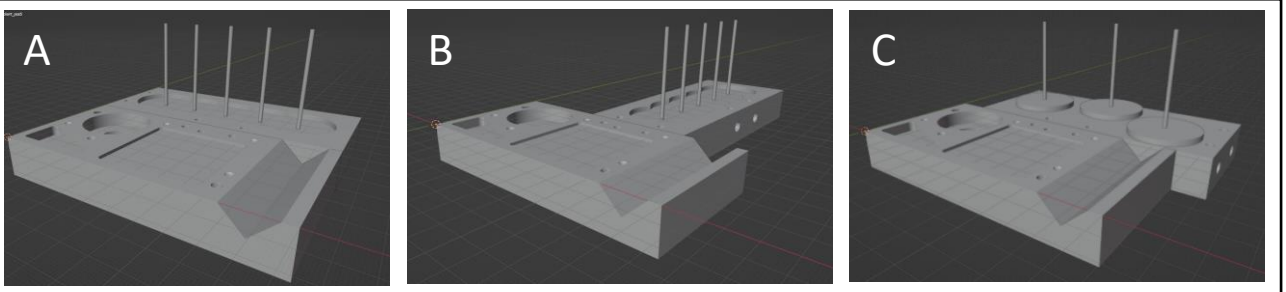

Figure 20. Implant positions as imported in Blender. A) Normal orientation tight-fit, B) Longitudinal orientation tight-fit, and C) No-fit experiments.

8.4.1. Marker pose registration

The location of the ArUco marker is virtualized in three coordinates: the center, a point in the direction of the surface's normal, and at the top of the ArUco surface. The three coordinates are:

- (72.5; 27.5; 0)
- (72.5; 27.5; 25)
- (72.5; 45; 0)

8.4.2. Point-to-point registration

The locations of the point to point registration points were predetermined and recreated in Blender.

8.4.3. Point cloud registration

The point cloud registration areas were brushed and extracted as separate surfaces.

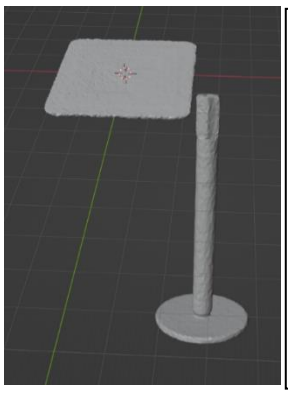

← Figure 22. Circular implant model. The 3D printed implant with attached ArUco marker was scanned with CBCT. The ArUco marker was manually aligned with Blender's x/y-plane.

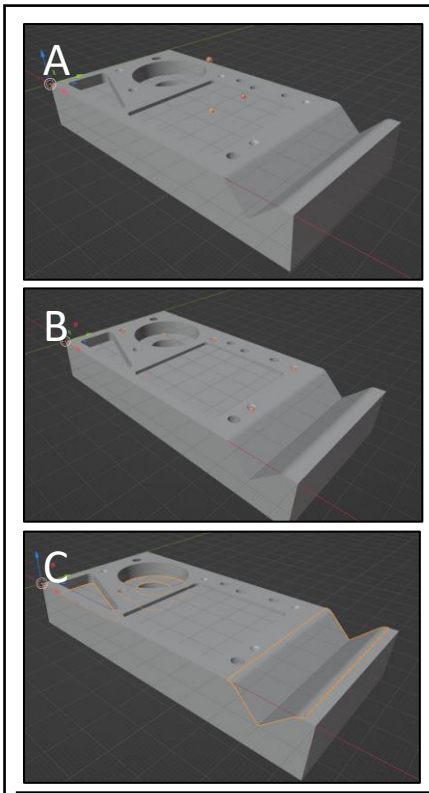

Figure 21. Registration preparations in Blender. A) Marker pose positions, B) point-to-point registration positions, C) point cloud areas.

9. Appendix B

9.1. ArUco marker tracking experiments – overhead lights

To utilize Holoma in a real clinical scenario in the future, it is important that Holoma functions properly in a real clinical environment. Overhead surgical lights that illuminate the surgical field is one of environmental factors that influences Holoma's functionality. Holoma should therefore be able to detect ArUco markers in these conditions and also be able to track the markers precisely. To measure ArUco detection and localization precision, the stationary and dynamic ArUco marker tracking experiments were

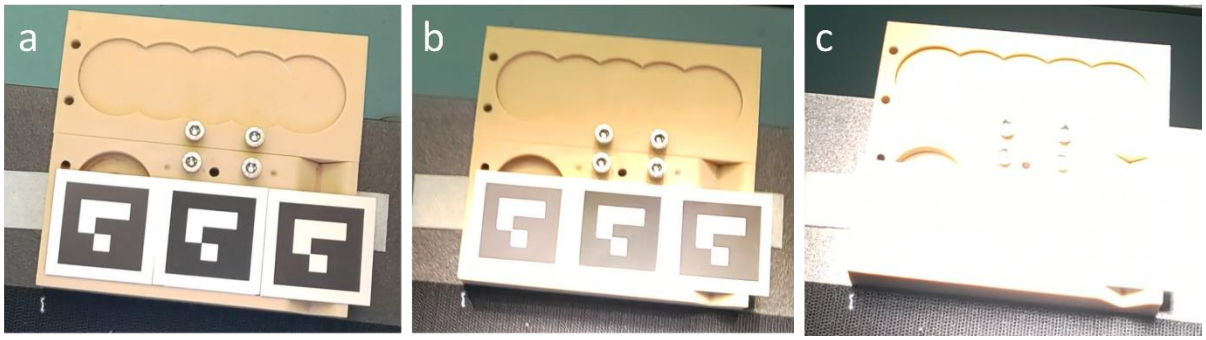

Figure 24 illustrates the effect of an overhead surgical lamp illuminating the markers. Markers of three different materials are shown (plastic with matte coated paint, metal, plastic) and A) shows normal lighting conditions, B) shows the markers while partially being illuminated, and C) shows what the Hololens camera sees when the markers are directly illuminated by the surgical lights.

conducted with overhead surgical lights illuminating the markers.

9.1.1. Methods

The stationary and dynamic experiments as described in section '4.2. ArUco marker and registration pointer tracking' were performed under partial illuminated conditions (as shown in figure 24B). The surgical lights were pointed as close to the markers as possible, while still being detected by Holoma.

9.1.2. Results

The stationary experiments showed that falsely detected motions of the ArUco markers ranged between 3.45 mm and 15.24 mm. The falsely detected motions of a stationary registration pointer increased to a maximum of 96.21 mm. The dynamic experiments resulted in falsely detected pointer movements between 6.66 mm and 30.51 mm. This

Table 9 shows the results of the marker and pointer precision experiments with overhead surgical lights partially illuminating the markers.

		Observed location	Median	1st quartile	3rd quartile	IQR	Min	Max	Range	ΔRange marker - pointer
Holoma	**stat m - stat c**	*Marker center*	2.96	2.72	4.11	**1.39**	0.66	4.11	**3.45**	**0.55**
		Pointer end	2.80	2.60	3.77	**1.17**	0.87	3.77	**2.90**	
	stat m - stat c user	*Marker center*	2.76	1.77	4.33	**2.56**	0.00	8.04	**8.04**	**1.88**
		Pointer end	2.93	1.74	3.69	**1.95**	0.00	6.16	**6.16**	
	stat m - left/right c	*Marker center*	4.03	3.00	8.46	**5.46**	0.00	15.24	**15.24**	**80.97**
		Pointer end	4.65	3.16	90.82	**87.66**	0.00	96.21	**96.21**	
	stat m - front/back c	*Marker center*	2.70	1.35	4.41	**3.06**	0.00	8.90	**8.90**	**0.16**
		Pointer end	2.96	1.56	4.44	**2.88**	0.00	8.74	**8.74**	
	stat m - up/down c	*Marker center*	1.24	0.92	7.34	**6.42**	0.00	13.85	**13.85**	**24.44**
		Pointer end	2.16	1.79	16.46	**14.67**	0.00	38.29	**38.29**	
Holoma	**dyn p - stat c**	*Pointer end*	2	1.29	3.46	**2.17**	0	6.66	**6.66**	
	dyn pl - stat c	*Pointer end*	3.18	1.38	5.57	**4.19**	0	11.32	**11.32**	
	dyn p - stat c user	*Pointer end*	11.35	4.81	16.52	**11.71**	0	30.51	**30.51**	
Brainlab	**stat p - stat c**	*Pointer end*	0.10	0.08	0.13	**0.05**	0.04	0.18	**0.14**	
	dyn p - stat c	*Pointer end*	0.25	0.19	0.33	**0.14**	0.06	0.53	**0.47**	
	stat p - dyn c	*Pointer end*	0.62	0.43	0.87	**0.44**	0.00	1.47	**1.47**	

was much larger when compared to similar experiments conducted with the Brainlab pointer, which resulted in falsely detected movements of 0.14 mm to 1.47 mm. Figure 25 and 26 show the results of the precision measurements that were performed.

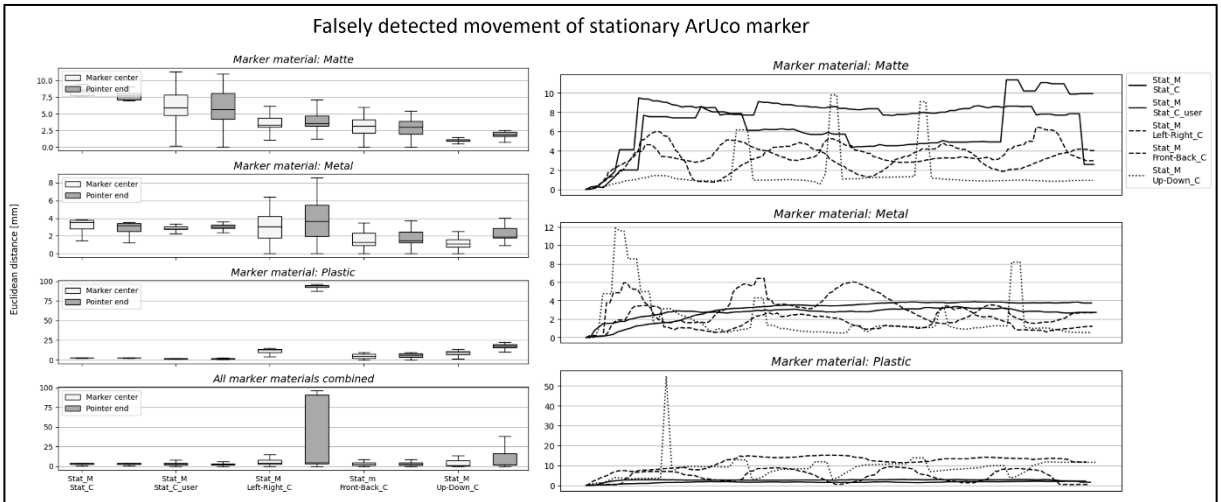

Figure 25 illustrates the results of the stationary ArUco marker tracking experiments. These results were deemed unreliable, as the markers were not detected for most of the experiments.

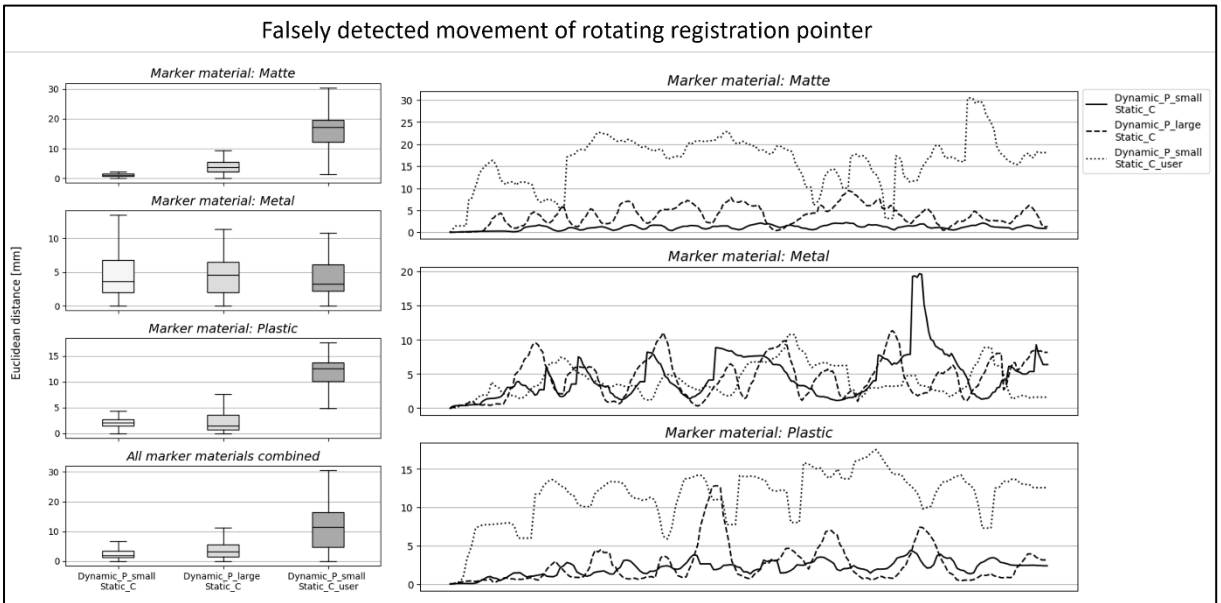

Figure 26 illustrates the results of the rotating pointer tracking experiments. These results were deemed unreliable, as the markers were not detected for most of the experiments.

9.1.3. Discussion

The results showed relative high errors in stationary and dynamic ArUco marker positions when overhead surgical light partially illuminated the markers. However, the partial illuminated experiments were not reliable, as the markers were not continuously detected by Holoma. The movement of the Hololens during the stationary experiments,

and the movement of the markers during the dynamic experiments, caused the surgical lights to fully reflect on the markers, most of the time. Therefore the results were not included in the thesis analysis.

9.1.4. Conclusion

Holoma is not able to detect ArUco markers in real surgical lighting conditions. Current surgical navigation systems are able to precisely determine a registration pointers position within a range of 1.5 mm.

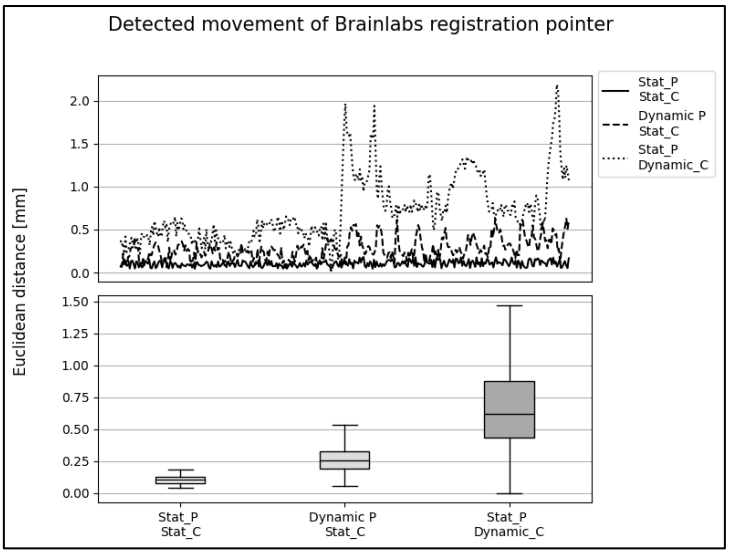

Figure 27 illustrates the results of the stationary and dynamic pointer tracking experiments with the Brainlab navigation system.